# Estimation of breaking wave properties and their interaction with a jacket structure

Ankit Aggarwal*[1], Hans Bihs[1], Seimur Shirinov[1], and Dag Myrhaug[2]

[1]Department of Civil and Environmental Engineering, Norwegian University of Science and Technology (NTNU), 7491 Trondheim, Norway
[2]Department of Marine Technology, Norwegian University of Science and Technology (NTNU), 7491 Trondheim, Norway

*Journal of Fluids and Structures*, 2019, **91** , pp. 102722.
DOI: http://dx.doi.org/10.1016/j.jfluidstructs.2019.102722

## Abstract

The numerical investigation of breaking wave interaction with jacket type offshore wind turbine substructures is quite challenging due to multiple jacket members and the complicated hydrodynamics of breaking waves around and inside the jacket. The present study is focused on investigating breaking wave forces and hydrodynamics on a jacket using a computational fluid dynamics (CFD) based numerical model. The breaking wave forces on a jacket mounted on a slope are investigated in a numerical wave tank. The experimental and numerical free surface elevations and wave forces are compared to validate the numerical model. The breaker indices and geometric profile properties for different wave steepness cases are correlated with force peaks. Further, the effect of changing the jacket location with respect to the wave breaker is investigated for different jacket locations for different wave steepness cases. In general, the force peaks are maximum when the fully grown breaker tongue impacts the jacket legs with large momentum. The influence of the jacket location on the wave-induced impact force rise time for both force peaks is also investigated in detail. The statistical analysis shows that the lognormal distribution is suitable to predict the breaking wave force statistics. The complex free surface features including the wave breaker tongue, secondary wave jet, chute like phenomenon and rejoining of the secondary wave jet with the free surface are observed during the interaction of breaking waves with the jacket. The role of horizontal velocity components in estimating the peak wave loads is further explored both deterministically and probabilistically.

**Keywords:** Jacket; CFD; breaking wave loads; breaker indices; breaker location

*Corresponding Author, Email: ankit.aggarwal@ntnu.no
*Postprint, published in Journal of Fluids and Structures,* doi:http://dx.doi.org/10.1016/j.jfluidstructs.2019.102722

# 1 Introduction

The increasing demand in developing technology for offshore wind energy has stimulated the research towards offshore wind turbine substructures that would be able to withstand harsh environmental conditions. Among the offshore wind turbine (OWT) substructures, monopiles are most widely used worldwide. Due to the proximity to the coast, monopiles are easy to fabricate, to transport and to install in shallow waters (EWEA , 2015). However, monopiles require more material tonnage in deeper water depths, where installation and transportation also become expensive (Damiani et al., 2016). Several studies have also shown that monopiles are progressively unfeasible as projects are located in deeper water depths and use larger turbine sizes (Musial et al., 2006; De Vries et al., 2011). In such scenarios, other substructures like jackets can be used. They can provide the needed structural stiffness by concentrating the mass away from the neutral axis (Damiani et al., 2016). Breaking wave loads are one of the most important environmental loads to be considered during the design of OWTs. The wave breaking process is generally initiated by changing water depths from deeper to shallower water. The breaking waves are characterized by the overturning wave crest. When the overturning wave crest impacts the structures with a large mass of water, it exerts high impact forces which can be crucial for the design of OWTs.

Semi-empirical formulas are applied in the offshore wind energy industry worldwide to estimate breaking wave loads by introducing slamming wave coefficients. Goda et al. (1966) suggested an additional impact load term in the Morison equation for breaking wave loads. Some experiments were conducted in the past to estimate the slamming coefficients for monopiles including the studies by Sarpkaya (1979); Sawaragi and Nochino (1984); Tanimoto and Shiota (1986); Apelt and Piorewicz (1987); Wienke et al. (2000); Irschik et al. (2004); Ros (2011); Burmester et al. (2017). The slamming coefficients estimated by these researchers have shown a considerable degree of scatter (from $\pi$ to $2\pi$). This scatter induces uncertainty in the calculation of breaking wave loads. All the above mentioned studies regarding slamming wave loads are limited to monopiles. Jacket structures are more complex due to multiple members, joints and different member orientations (Aashamar, 2012). The strong non-linear wave hydrodynamic processes like wave shoaling, wave breaking, wave decomposition and interaction of the multiple members and joints in the jacket structure make it quite challenging to accurately estimate the breaking wave loads on the jacket members (Loukogeorgaki et al., 2016). The design guidelines (ISO 21650 (2007), DNVRP-C205 (2010), API RP 2A-WSD (2007) and ISO 19902 (2007)) provide only limited information about the jacket design under breaking wave loads. Arntsen and Gudmestad (2014) conducted experiments to measure the breaking wave loads due to plunging wave breakers on a jacket structure. They measured the structural response in their experiments. Later, studies were conducted by Ying et al. (2018) and Jose et al. (2016) to estimate the wave-induced breaking wave loads from the experimentally measured structural response.

Numerical modelling with Computational Fluid Dynamics (CFD) can be used to study breaking waves and associated wave forces. Many important hydrodynamic flow details can be modelled with CFD, which are difficult to measure in the experiments, by the use of the higher-order numerical schemes, sharp representation of the free surface and accurate closure of the turbulence. Several researchers have applied CFD in the past to study breaking waves and associated forces (Lin and Liu, 1998; Zhao et al., 2004; Hieu et al., 2004; Christensen, 2006; Jacobsen et al., 2012; Mo et al., 2013; Bihs et al., 2016*b*; Alagan Chella et al., 2017).

Christensen et al. (2005) modelled total wave forces and wave run-up due to breaking waves in shallow waters with a Navier-Stokes (NS) solver and the volume-of-fluid (VOF) method. Bredmose and Jacobsen (2010) performed simulations for a monopile with the open-source software OpenFOAM based on the NS equations and the VOF method for free surface without an explicit turbulence model. In the simulation, breaking waves were generated using the focussed wave group method. A similar approach was employed by Bredmose and Jacobsen (2011) to study the vertical wave impacts on offshore wind turbine inspection platforms with the OpenFOAM. Choi et al. (2015) analysed the breaking wave loads on vertical and inclined cylinders with CFD to study the dynamic amplification factor due to structural response. Their model is based on NS equations and it employs the VOF method for the free surface. Kamath et al. (2016) studied the effect of the wave breaker location on the wave impact forces for a monopile by using the Reynolds-Averaged Navier-Stokes (RANS) equations based numerical model REEF3D. They reported that the maximum wave impact forces are obtained when the breaking wave tongue impacts the cylinder just below the wave crest. Hildebrandt and Schlurmann (2012) investigated breaking wave loads on tripod legs using ANSYS-CFX and compared their results for free surface elevation and wave forces with the experiments. Their numerical results showed a good agreement with experimental data. Jose and Choi (2017) conducted a numerical study to model the breaking wave forces on jacket structures. They also estimated the slamming coefficients for local jacket members, and compared their numerical results with the experiments by Arntsen and Gudmestad (2014) to validate their numerical model. The numerical results were fairly accurate, although some peaks in the wave impact forces were not captured correctly and the breaking wave kinematics was underresolved as the overturning jet was absent. The wave breaker location can have a significant effect on the wave impact loads due to the multiple scenarios of the jacket-breaker tongue interaction. To the best of the authors' knowledge, there have been no CFD studies to investigate the effect of the breaker location on the wave impact forces for a jacket structure.

The goal of the present work is to study the breaking wave characteristics and to investigate the effect of the breaker location on wave impact loads for a jacket structure. The numerical simulations are performed with the CFD module of the open-source hydrodynamics model REEF3D (Bihs et al., 2016*a*; Bihs and Kamath, 2017). In the past, the numerical model has been successfully applied to various coastal and marine engineering problems including breaking waves and breaking wave forces (Aggarwal et al., 2016, 2018*a*; Bihs et al., 2016*b*; Alagan Chella et al., 2017; Ahmad et al., 2018). The numerical model employs higher-order numerical schemes capable of capturing the complete breaking process. It is quite difficult for numerical models to generate an accurate mesh around the jacket structure due to the structural complexity of the jacket. The current approach uses a ghost cell immersed boundary method (GCIBM) to implement an accurate mesh around the jacket. In the current study, the numerical model is first validated for the breaking wave interaction with the jacket structure by comparing the numerical free surface elevation at different wave gauge locations with the experiments by Arntsen and Gudmestad (2014). The numerical breaking wave force is compared with the experimental wave force for validation purposes. Two-dimensional simulations are carried out in order to investigate the breaking wave characteristics and wave crest deformations including the breaking height index, the breaker depth index and the geometric wave profile properties for different incident wave steepnesses. Three-dimensional simulations are carried out in order to estimate the breaking wave loads under four different wave impact scenarios. The jacket is placed at four different distances with respect to the breaker loca-

tion and these scenarios are evaluated for four different incident wave steepnesses each. The evolution of wave harmonics during wave shoaling, wave breaking and wave decomposition processes and their effect on slamming loads is analysed. The role of the breaker location and the incident wave steepness on the rise-time of the slamming loads is investigated for all cases. Various free surface flow features during the interaction of breaking waves with the jacket structure including the primary wave jet, rejoining of the primary wave jet with the free surface and generation of the secondary wave jet are also discussed. Further, the statistics of the slamming load rise-time, breaking wave force and horizontal velocity components are further investigated by estimating the most suitable probabilistic distribution fit.

# 2 Numerical Model

## 2.1 Governing Equations

The open-source hydrodynamics model REEF3D (Bihs et al., 2016*a*; Bihs and Kamath, 2017) based on the Reynolds-Averaged Navier-Stokes equations (RANS) defined for incompressible fluids is used. The governing momentum conservation equations and the continuity equation are:

$$\frac{\partial u_i}{\partial x_i} = 0 \tag{1}$$

$$\frac{\partial u_i}{\partial t} + u_j \frac{\partial u_i}{\partial x_j} = -\frac{1}{\rho}\frac{\partial P}{\partial x_i} + \frac{\partial}{\partial x_j}\left[(\nu + \nu_t)\left(\frac{\partial u_i}{\partial x_j} + \frac{\partial u_j}{\partial x_i}\right)\right] + g_i \tag{2}$$

where $u_i$ is the velocity averaged over time $t$, $\rho$ is the fluid density, $P$ is the pressure, $\nu$ is the kinematic viscosity, $\nu_t$ is the eddy-viscosity, $i$ and $j$ denote the indices in x and y direction, respectively and $g_i$ is the acceleration due to gravity.

For the spatial discretization, the fifth-order finite difference Weighted Essentially Non-Oscillatory (WENO) scheme in multi-space dimensions is used (Jiang and Shu, 1996). The third-order TVD Runge Kutta scheme is implemented for time discretization (Shu and Oscher, 1988). Adaptive time stepping is applied in order to control the CFL-number and to compute the time step size (Griebel et al., 1998). The pressure in the Navier-Stokes equations is calculated using the projection method (Chorin, 1968). The HYPRE conjugate gradient solver in combination with the multigrid preconditioning is utilized to solve the Poisson pressure equation (Falgout and Yang, 2002). The present study uses the $k-\omega$ model (Wilcox, 1994) along with the RANS equations for turbulence closure. The numerical model employs a Cartesian grid approach in order to apply higher-order discretization schemes. A ghost cell immersed boundary method (GCIBM) is implemented to consider irregular and non-orthogonal solid boundaries (Berthelsen and Faltinsen, 2008). This approach allows straightforward meshing around the complex jacket structure. For capturing the free surface, the level set method approach (Osher and Sethian, 1988) is used. The level set function gives the closest distance to the interface and the two phases are distinguished by the change of the sign. The function can be written as:

$$\phi(\vec{x},t)\begin{cases} > 0 & if\ \vec{x} \text{ is in phase 1} \\ = 0 & if\ \vec{x} \text{ is at the interface} \\ < 0 & if\ \vec{x} \text{ is in phase 2} \end{cases} \tag{3}$$

### 2.2 Wave force computation

The total wave force ($F$) in the numerical model is calculated by integrating the pressure and the normal component of viscous stress tensor $\tau$ over the surface $\Omega$ of the structure. This procedure is performed discretely by evaluating the pressure $p$ and $\tau$ for all individual cell surface of the structure:

$$F = \int_{\Omega} (-\mathbf{n}p + \mathbf{n}.\tau) d\Omega \tag{4}$$

## 3 Results and discussion

### 3.1 Computational setup

The experiments were conducted as a part of the WaveSlam project (Arntsen and Gudmestad, 2014) at the large wave flume (GWK) in Hannover with the aim to study the breaking wave forces on a jacket structure. The experiments were conducted at a scale of 1:8 with the Thornton bank wind farm, which is located on the Belgian coast in water ranging from 12 m to 27 m deep. The large wave flume in Hannover is 300 m long, 5 m wide and 7 m deep. The slope of the bottom of the ramp is 1:10. The diameter of each jacket member is 0.14 m. The jacket is located 200 m from the wave generator at the end of the slope. Incident regular waves with heights $H$ between 1.60–1.70 m and periods $T$ between 4.0–6.0 s are generated. To simulate the experimental setup, the numerical simulations are conducted in two parts to reduce computational costs. First, the numerical simulation is conducted in a two-dimensional (2D) numerical wave tank (NWT) without jacket. The 2D NWT is 100 m long and 7 m deep with a water depth $d$ of 4.3 m (Fig. 1a) to model the wave propagation and the breaking process. The waves in the 2D NWT are generated with the relaxation method (Mayer et al., 1998) and absorbed with the active wave absorption method.

The numerical simulations with the jacket structure are conducted in a 3D NWT. The 3D NWT is 38 m long, 5 m wide and 7 m deep. The water depth is $d = 4.3$ m and the jacket with each members's diameter $D = 0.14$ m is mounted on top of the slope as in the experiments (Fig. 1b). The jacket can be seen in Fig. 1c. The waves at a distance of -28 m from the wavemaker in the 2D NWT are reconstructed in the 3D NWT at $x$ = -28 m (beginning of the 3D NWT) using the free surface reconstruction technique (Aggarwal et al., 2018*b*). The reconstructed waves in the 3D NWT are then identical to the waves in the 2D NWT. The wave gauges are placed at $x$ = -28 m (W1), -7 m (W2), -5 m (W3), -3 m (W4), -2 m (W5), 1 m (W6) and 5 m (W7) to measure the free surface elevations; velocity probes are placed at the free surface at $x$ = -23 m (P1), -16.5 (P2), -2 m (P3), -1 m (P4), 0 m (P5), 0.5 m (P6), 3.5 m (P7) and 7 m (P8) to measure the particle velocities. The list of simulation cases for the validation of the numerical model and to investigate the effect of breaker location can be seen in Table 1 and Table 2, respectively.

### 3.2 Validation of the numerical model

**Grid convergence study** The grid convergence study is carried out for the free surface elevation measured at the wave gauge at $x$ = -2 m (see Fig. 1 for the coordinate system). The numerical simulations are performed with a wave height $H = 1.60$ m and a wave period of $T = 5.55$ s (case S1, Table 1) for four different grid sizes $dx = 0.20$ m, 0.10 m, 0.05 m and

| No. | Wave height $H(m)$ | Wave period $T(s)$ | Steepness $s$ | Breaking point $x_b(m)$ |
|---|---|---|---|---|
| S1 | 1.60 | 5.55 | 0.033 | 1.64 |
| S2 | 1.50 | 4.60 | 0.045 | 1.45 |
| S3 | 1.60 | 4.60 | 0.048 | 1.10 |
| S4 | 1.70 | 4.60 | 0.051 | 0.90 |

Table 1: Simulation cases for 2D NWT with different incident wave steepnesses

0.025 m. Fig. 2a presents the comparison of the numerical and experimental wave free surface elevation versus time with different grid sizes $dx$ for case S1 at W5 ($x$ = -2 m). It appears that the numerical results with $dx$ = 0.20 m and 0.10 m underestimate the peak wave amplitude by 10 % and 8 %, respectively. Also, the location of the wave peak in the time-series is not accurately presented. The error in the computation of the wave peak locations with $dx$ = 0.20 m and 0.10 m are 0.11 % and 0.09 %, respectively. On refining the grid size to $dx$ = 0.05 m, the peak wave amplitude errors and peak wave amplitude location errors between the experimental and numerical results reduce to 2.6 % and 0.03 %, respectively and the numerical model is able to represent the experimental free surface elevation with a reasonable accuracy at this grid size $dx$ = 0.05 m. On the refinement of the grid size to $dx$ = 0.025 m, the results are not improved further, indicating that the numerical results are converged at $dx$ = 0.05 m. Thus, $dx$ = 0.05 m is chosen for the following simulations. Fig. 2b presents the peak wave amplitude errors and peak wave amplitude location errors between the experimental and numerical results versus $dx$. It can be seen that both errors reduce significantly on refining $dx$ from 0.20 m to 0.05 m and this decrement becomes insignificant on the further refinement of $dx$ to 0.025 m. Fig. 3 presents the comparison of the numerical and experimental wave free surface elevation versus time at different wave gauges (W3, W4 and W5) for case S1 with $dx$ = 0.05 m. The time-step is calculated based on the CFL number in the numerical model (Bihs et al., 2016*a*). The numerical model is able to model and compute the free surface elevation at different wave gauges located over the slope. The wave propagation over slopes is characterized by a complex wave shoaling process which is correctly represented by the numerical model. The peaks of the wave amplitude and locations of the amplitude peaks are accurately modelled. The wave crests become sharper compared to the wave troughs due to the shallower water depths during wave shoaling as shown by the both experimental and numerical results.

| Cases | Steepness $s$ | Wave height $H$ (m) | Wave period $T$ (s) | $x$ (m) |
|---|---|---|---|---|
| A1 | 0.048 | 1.60 | 4.60 | 0 |
| A2 | | 1.60 | 4.60 | 0.5 |
| A3 | | 1.60 | 4.60 | 1.0 |
| A4 | | 1.60 | 4.60 | 1.5 |
| B1 | 0.051 | 1.70 | 4.60 | 0 |
| B2 | | 1.70 | 4.60 | 0.5 |
| B3 | | 1.70 | 4.60 | 1.0 |
| B4 | | 1.70 | 4.60 | 1.5 |
| C1 | 0.033 | 1.60 | 5.55 | 0 |
| C2 | | 1.60 | 5.55 | 0.5 |
| C3 | | 1.60 | 5.55 | 1.0 |
| C4 | | 1.60 | 5.55 | 1.5 |
| D1 | 0.035 | 1.70 | 5.55 | 0 |
| D2 | | 1.70 | 5.55 | 0.5 |
| D3 | | 1.70 | 5.55 | 1.0 |
| D4 | | 1.70 | 5.55 | 1.5 |

Table 2: Simulation cases for the investigation of effect of wave breaker location on breaking wave forces in 3D NWT

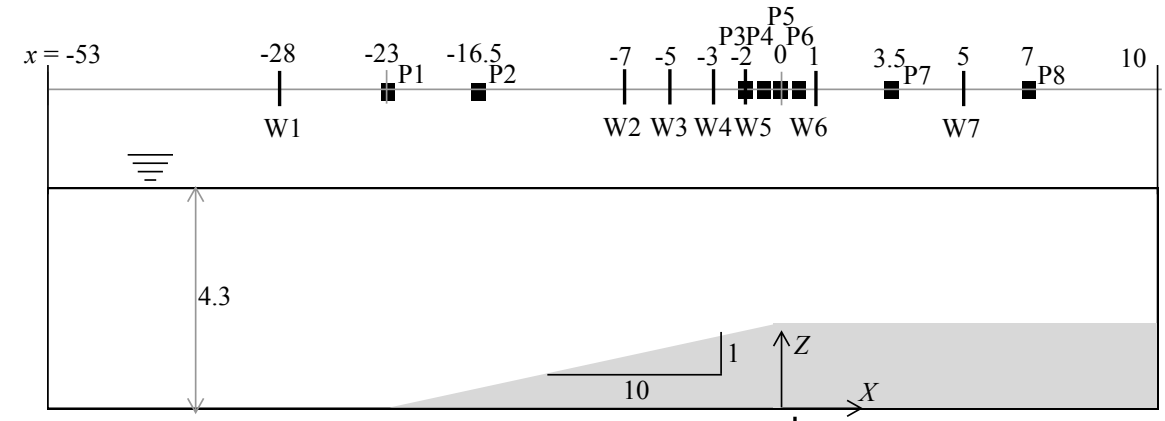


(a)

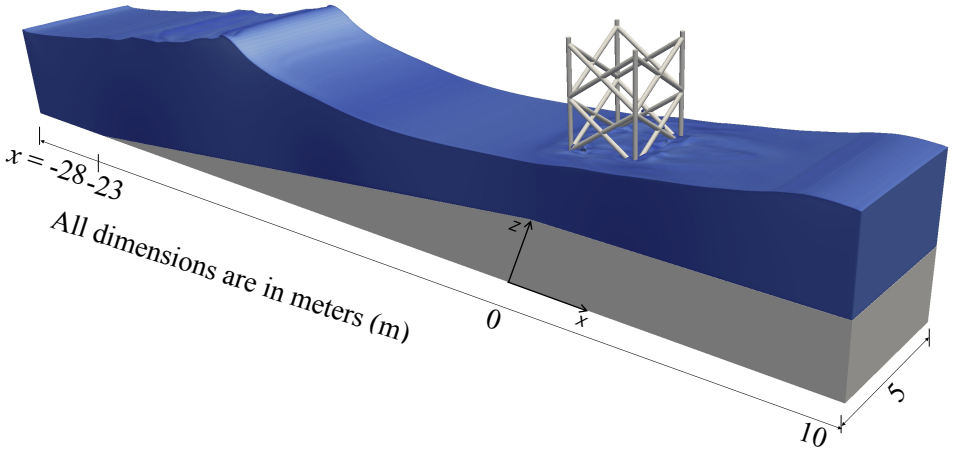


(b)

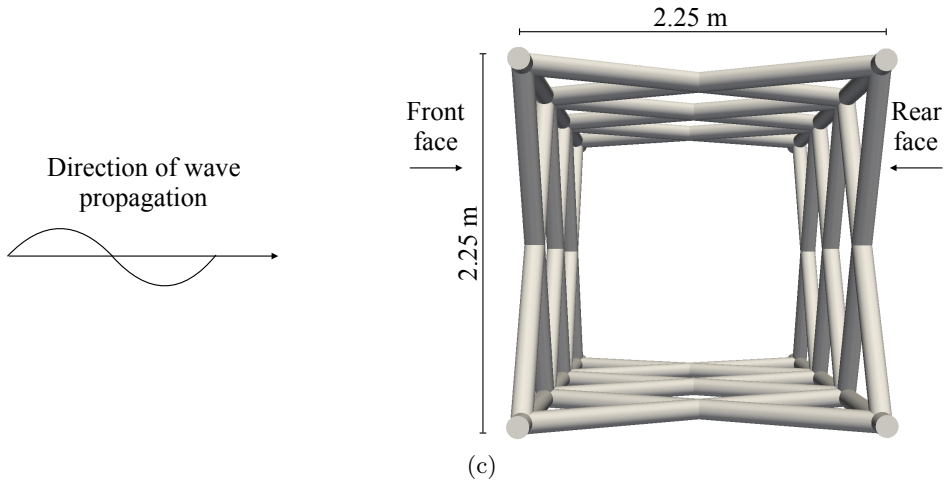


(c)

Figure 1: Setup of the numerical wave tank used in the present study (a) 2D NWT (b) 3D NWT (c) jacket

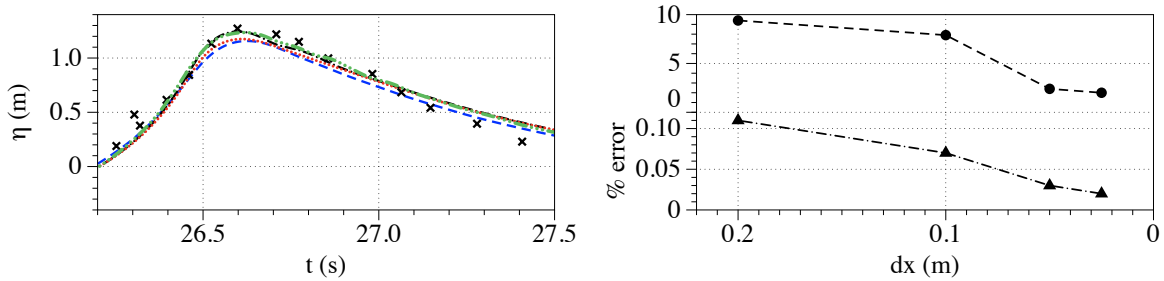


(a) (b)

Figure 2: Grid convergence study for wave free surface elevation at $x$ = -2 m (W5) (a) $\eta$ at different $dx$; black crosses for experimental; green dotted for $dx$ = 0.025 m; black dotted for $dx$ = 0.05 m; red dotted for $dx$ = 0.10 m; blue dotted for $dx$ = 0.20 m (b) % errors versus $dx$; dots for peak wave amplitude error; triangles for peak wave amplitude location error

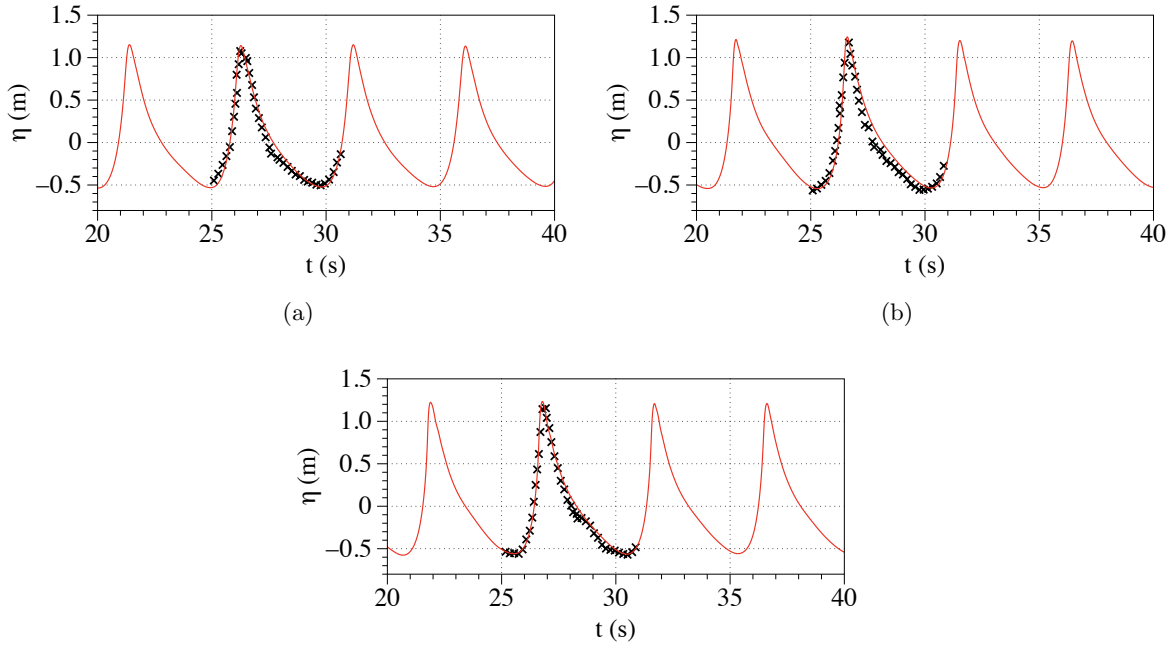


(a) (b)

(c)

Figure 3: Comparison of the experimental and numerical wave free surface elevation time-series for case S1 at (a) W3 ($x$ = -5 m) (b) W4 ($x$ = -3 m) (c) W5 ($x$ = -2 m). Red solid line presents numerical; black crosses for experimental

**Validation of breaking wave force** After the numerical model is validated for the free surface elevation, the validation study for the total breaking wave force on the jacket is performed. The simulations are run for cases S1, S2, S3 and S4 with $dx$ = 0.05 m. The jacket is placed exactly at the location as in the experiments. Fig. 4 presents a comparison of the

normalized numerical and experimental breaking wave force versus time for cases S1-S4 with $dx = 0.05$ m. Wave steepness is given by:

$$s = \frac{2\pi H}{gT^2} \tag{5}$$

Waves impact the jacket structure at different locations for cases S1-S4 as shown in Fig. 5. The wave forces are normalized with the following equation (Eq. 3.2.2):

$$\hat{F} = \frac{F}{\rho g D^3} \tag{6}$$

where $\rho$ is the water density and $D$ is the diameter of the jacket members.

The numerical model is able to compute the total breaking wave loads on the jacket structure with a good accuracy as seen in Figs. 4a, 4b, 4c and 4d. The first and second force peaks are estimated with errors of 2.3 % and 2.7 % for case S1, 2.9 % and 2.5 % for case S2, 1 % and 1.7 % for case S3 and with errors of 0.8 % and 2.7 % for case S4, respectively. The breaking waves impact the front face of the jacket first which leads to the first peak. Then, they interact with the rear face, resulting in the second force peak in the force time series (Fig. 5). There are some minor discrepancies in the troughs of the numerical and experimental wave force signal, but since the focus of the present study is to investigate the peak breaking wave loads, further simulations are continued with $dx = 0.05$ m. Further, in order to verify the repeatability of numerical simulations, 4 trial runs are conducted for case S4 (Fig. 4e). The numerical results with all of the trial runs are almost the same and are in a good agreement with the experimental data, which further verifies the repeatability of the numerical results for breaking wave forces on jackets.

**Spatial evolution of horizontal velocity** Fig. 6 presents the normalized horizontal velocity versus the distance along the NWT for cases S1 to S4. The horizontal velocity components are normalized according to the following equation:

$$\hat{u} = \frac{u}{\sqrt{gd}} \tag{7}$$

The horizontal velocity component is highest for the waves with the largest wave steepness. For all cases, the maximum horizontal velocity is attained at the breaker tongue during the wave breaking process. In general, the velocity increases during shoaling up to the point where the wave crest becomes unstable and the wave breaks. For case S4 (largest wave steepness case), the maximum $\hat{u}$ is larger by almost 23 % compared to case S1 (lowest wave steepness case). Due to the larger horizontal velocity at wave breaking, waves impact the jacket with a larger momentum resulting in larger wave-induced impact loads. After the wave breaking has occurred, the horizontal velocity reduces due to the loss of wave energy during the breaking process. This process is evidently similar for all cases (S1 to S4).

Figure 6: Variation of the horizontal velocity component during the breaking wave interaction with the jacket for cases S1-S4. White circles for case S1; black circles for case S2; white squares for case S3; black squares for case S4

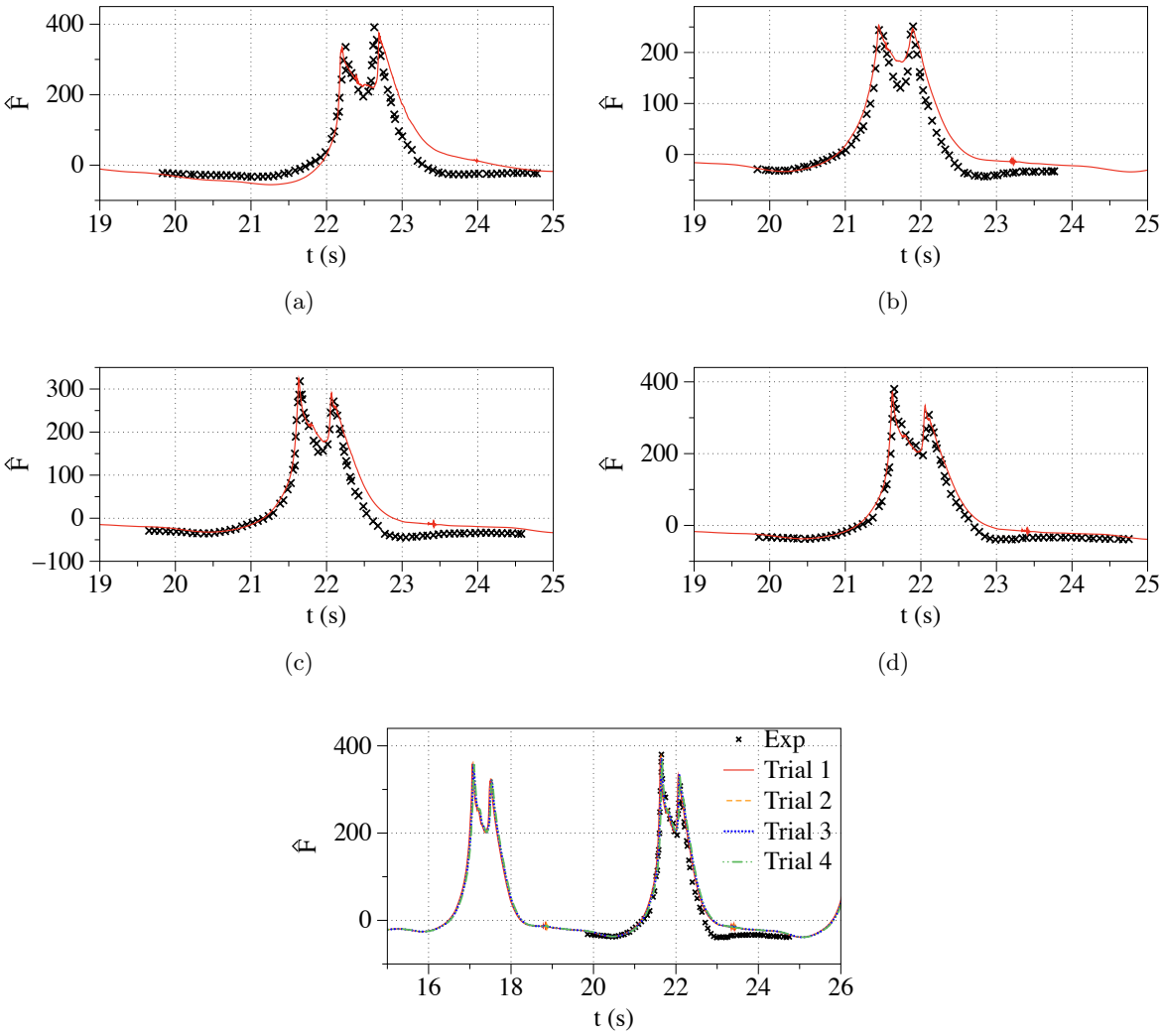


Figure 4: Comparison of the experimental and numerical normalised breaking wave force time-series for case (a) S1 ($s$ = 0.033) (b) S2 ($s$ = 0.045) (c) S3 ($s$ = 0.048) (d) S4 ($s$ = 0.051) (e) S4 ($s$ = 0.051) with multiple numerical runs for verifying the repeatability of numerical simulations under dynamic wave loadings. For Figs. 4a to 4d: Red solid line presents numerical results and black crosses show experimental results

### 3.3 Breaking wave characteristics and wave profile geometric properties

The breaker depth index ($\gamma_b$) and breaker height index ($\Omega_b$) are used to investigate the breaking characteristics. They are defined as:

$$\gamma_b = \frac{H_b}{d_b}; \Omega_b = \frac{H_b}{H_o} \tag{8}$$

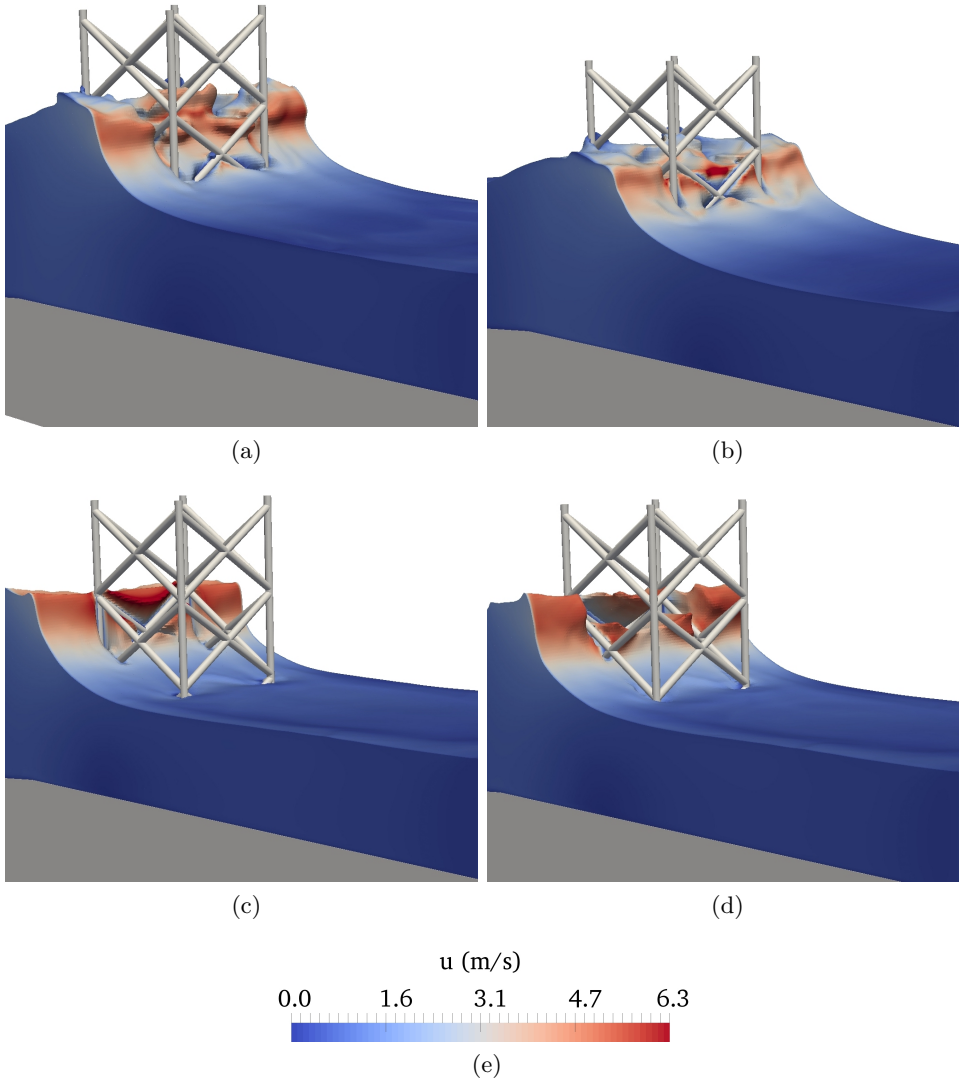


Figure 5: Different wave impact locations for case (a) S1 ($s$ = 0.033) at $t$ = 22.16s (b) S2 ($s$ = 0.045) at $t$ = 22.21s (c) S3 ($s$ = 0.048) at $t$ = 21.33s (d) S4 ($s$ = 0.051) at $t$ = 21.47s.

where $d_b$ is the depth at breaking, $H_b$ is the local wave height at breaking and $H_o$ is the offshore input wave height.

Kjeldsen and Myrhaug (1978) defined the steepness and asymmetry parameters for the local wave crest asymmetry at breaking: the wave crest front steepness ($\varepsilon$), the wave crest rear steepness ($\delta$), the horizontal asymmetry factor ($\mu$) and the vertical asymmetry factor ($\lambda$) as seen in Fig. 7. The present study uses these steepness and asymmetry parameters to study the geometric properties of breaking waves over different slopes.

Fig. 8 presents the breaker depth index ($\gamma_b$) (Fig. 8a) and the breaker height index ($\Omega_b$) (Fig. 8b) versus the distance at which the waves break ($x_b$) for cases S1–S4. It is observed that $\gamma_b$ and $\Omega_b$ decrease as $x_b$ increases. When the wave steepness increases, the breaking location shifts offshore (i.e., $x_b$ decreases) as observed in Table 1 and Fig. 1, and the waves break with a larger breaker height $H_b$. The waves with lower steepness $s$ break more onshore

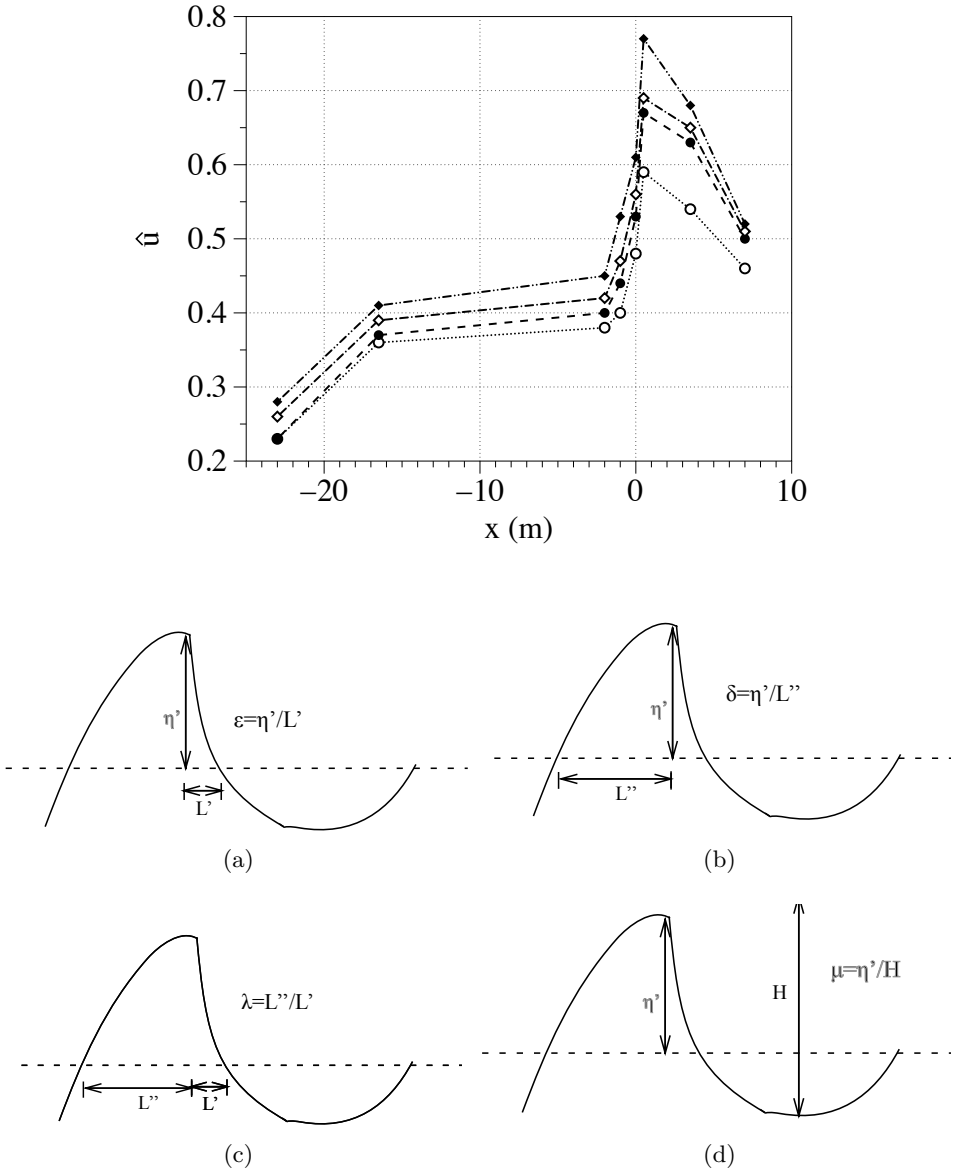


Figure 7: Definitions of wave profile geometry (Kjeldsen and Myrhaug, 1978) (a) crest front wave steepness $\varepsilon$; (b) crest rear wave steepness $\delta$; (c) vertical asymmetry factor $\lambda$; (d) horizontal asymmetry factor $\mu$

at shallower water depths and experience more deformation. In all the cases $\Omega_b > 1$, which means that the waves grow more than the incident $H$ during the shoaling process and have a higher $H_b$ than incident $H$ for all cases. Figs. 9a, 9b, 9c and 9d present the crest front wave steepness ($\varepsilon$), the crest rear wave steepness ($\delta$), the horizontal asymmetry factor ($\mu$) and the vertical asymmetry factor ($\lambda$), respectively, versus $x_b$ for cases S1–S4. In general, the crest front steepness ($\varepsilon$) and the crest rear steepness ($\delta$) decrease (with maximum at $x_b = 1.1$ m) as $x_b$ increases (as the wave breaking location shifts onshore). The wave crest becomes steeper and more skewed, when waves propagate for longer distances over the flat part of the slope. It

is noticed from Figs. 9c and 9d that the values of $\lambda$ almost remain the same with changes in $x_b$ except at $x_b = 1.1$ m, but the values of $\mu$ decrease slightly as $x_b$ increases. The maximum value of $\delta$ and the minimum value of $\lambda$ at $x_b = 1.1$ m could possibly be due to the interaction of the almost vertical wave crest with the front legs of the jacket for case S3 ($s = 0.048$) as shown in Fig. 5c. The front face of the wave crest becomes very steep without much change in the rear face of the wave crest due to more offshore wave breaking.

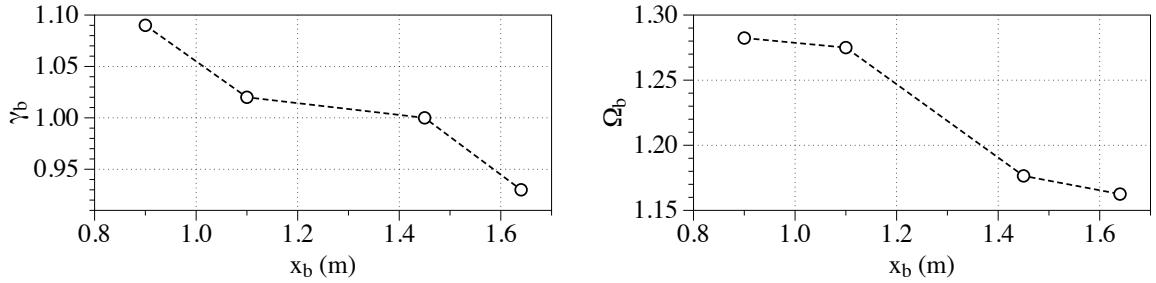


Figure 8: Variation of the breaker indices versus wave breaking location $x_b$ (a) breaker depth index $\gamma_b$ (b); breaker height index $\Omega_b$

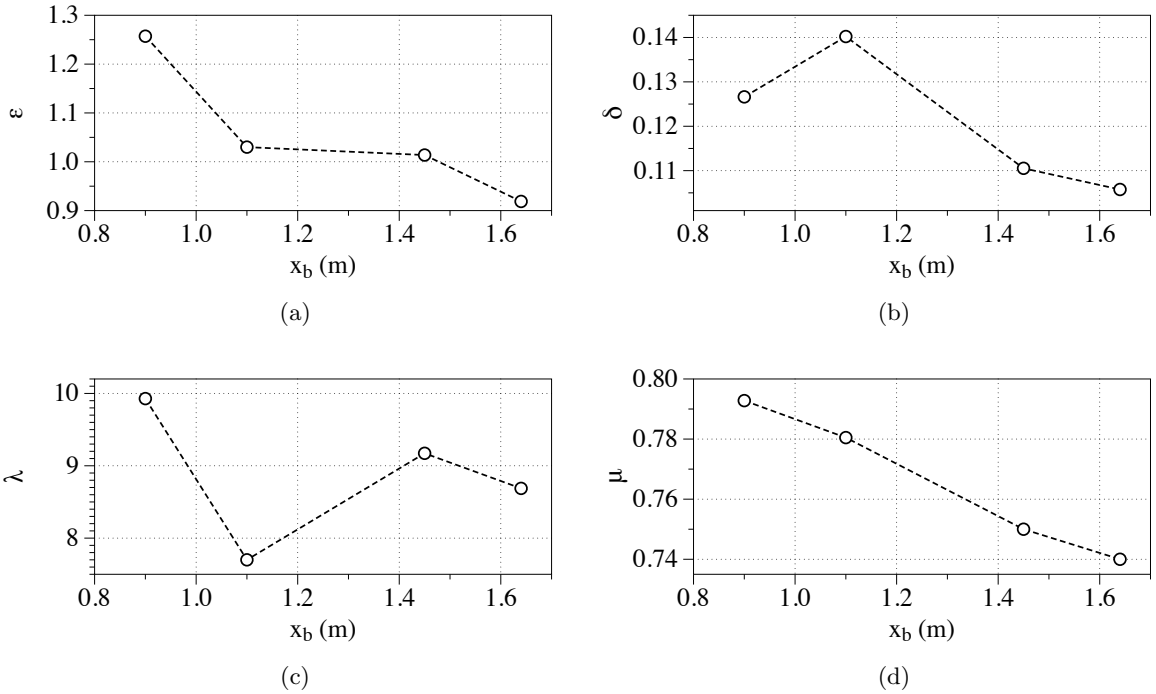


Figure 9: Variation of the wave profile geometric parameters versus wave breaking location $x_b$ (a) crest front wave steepness $\varepsilon$; (b) crest rear wave steepness $\delta$; (c) vertical asymmetry factor $\lambda$; (d) horizontal asymmetry factor $\mu$

Fig. 10 shows the bar representation of the first and second force peaks versus breaker depth index ($\gamma_b$), the breaker height index ($\Omega_b$), the crest front wave steepness ($\varepsilon$), the crest rear wave steepness ($\delta$), the horizontal asymmetry factor ($\mu$) and the vertical asymmetry factor ($\lambda$) for cases S1–S4. Both, the first and second force peaks follow the similar trend for $\gamma_b$ (Fig. 10a). They are reduced by almost 24 % and 36 %, respectively, when $\gamma_b$ increases to 1.02. Both force peaks increase on the further increment of $\gamma_b$. A similar trend is observed for the force peak value as $\Omega_b$ increases (Fig. 10b). This is due to the shift in the wave breaking location towards deeper water as discussed in the previous section, demonstrating that the wave breaking location plays an important role in estimating the wave-induced impact force peaks. When the overturning wave crest impacts the front legs of the jacket, the first force peak is larger than the second one, while when the overturning wave crest impacts the rear legs of the jacket, the second force peak is larger than the first one. The trends of force peaks $\hat{F_p}$ versus crest front wave steepness ($\varepsilon$) and the crest rear wave steepness ($\delta$) are similar to that of the breaker indices (Figs. 10c and 10d, respectively). For the horizontal asymmetry factor ($\mu$) and the vertical asymmetry factor ($\lambda$), the peak forces first increase, then decrease to the minimum value and then increase again on the further increment of $\mu$ and $\lambda$ (Figs. 10e and 10f, respectively). The wave profile geometric properties represent the deformation, i.e., the asymmetry and skewness of the wave crest profile, which further depend on the incident wave steepness and wave breaking location.

When waves approach the shallower water depths, their wave height and wave length change. The wave length becomes shorter and the wave height and wave energy increase during the shoaling process. This process continues until the fluid particle velocity exceeds the wave crest velocity which leads to wave breaking. Fig. 11 presents the computed free surface profile with velocity variations during the wave propagation over the slope at t = 22.7 s, 22.9 s, 23.05 s, 23.2 s, 23.27 s and 23.39 s, respectively. When the waves propagate over the slope, they undergo shoaling which is observed by the increase in wave crest height. As the waves propagate further over the slope, the wave crest becomes almost vertical at the onset of wave breaking as seen in Fig. 11a; a small water jet is generated at the wave crest and the profile of the wave crest becomes highly deformed and asymmetric. When the fluid particle velocity at the wave crest exceeds the wave celerity, an overturning motion of the wave crest is induced (Fig. 11b). The overturning wave crest breaks with the encasement of an air pocket (Fig. 11c), referred to as the splash-up phenomenon and another small jet of water in the downstream direction is generated (Figs. 11d, 11e and 11f).

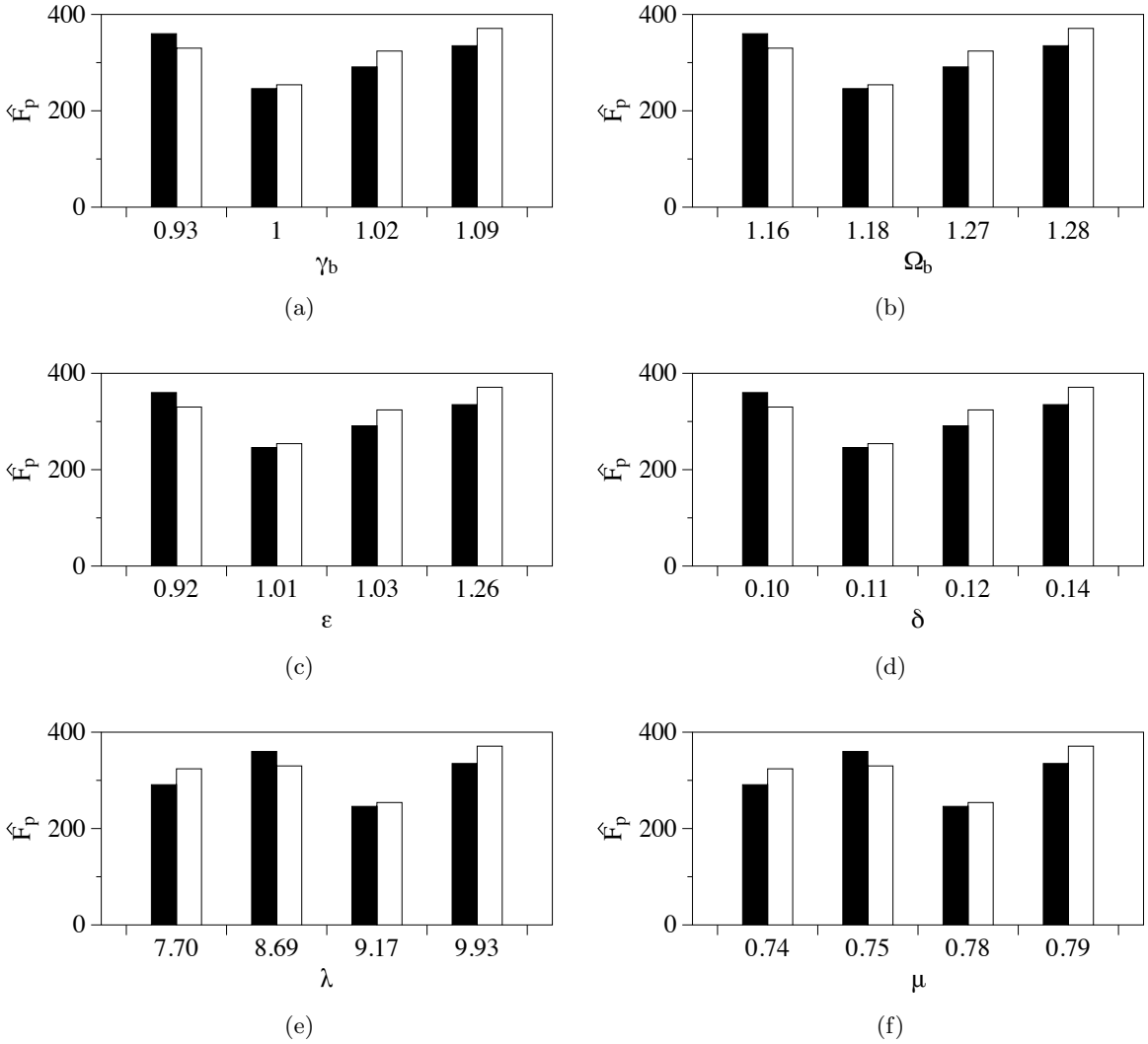


Figure 10: Bar representation of the first and second force peaks versus (a) breaker depth index $\gamma_b$ (b) breaker height index $\Omega_b$ (c) crest front wave steepness $\varepsilon$; (d) crest rear wave steepness $\delta$; (e) vertical asymmetry factor $\lambda$; (f) horizontal asymmetry factor $\mu$. White bar for first force peak and black bar for second force peak

### 3.4 Influence of jacket location with respect to the breaker location

The wave breaker location with respect to the OWT substructures has a significant effect on the magnitude of slamming wave loads. This has been shown previously by Irschik et al. (2004) and Kamath et al. (2016) for monopiles. This section of the paper is focused on exploring the effect of changing the distance of the jacket with respect to the wave breaking location on the breaking wave forces and the associated properties. Four different jacket locations are investigated for four different incident wave steepnesses. The list of the simulation cases for different wave loading cases can be seen in Table 2. The value of $x$ is 0 when the front legs of the jacket are placed at the start of the flat part of the seabed (refer to Fig. 1 for details).

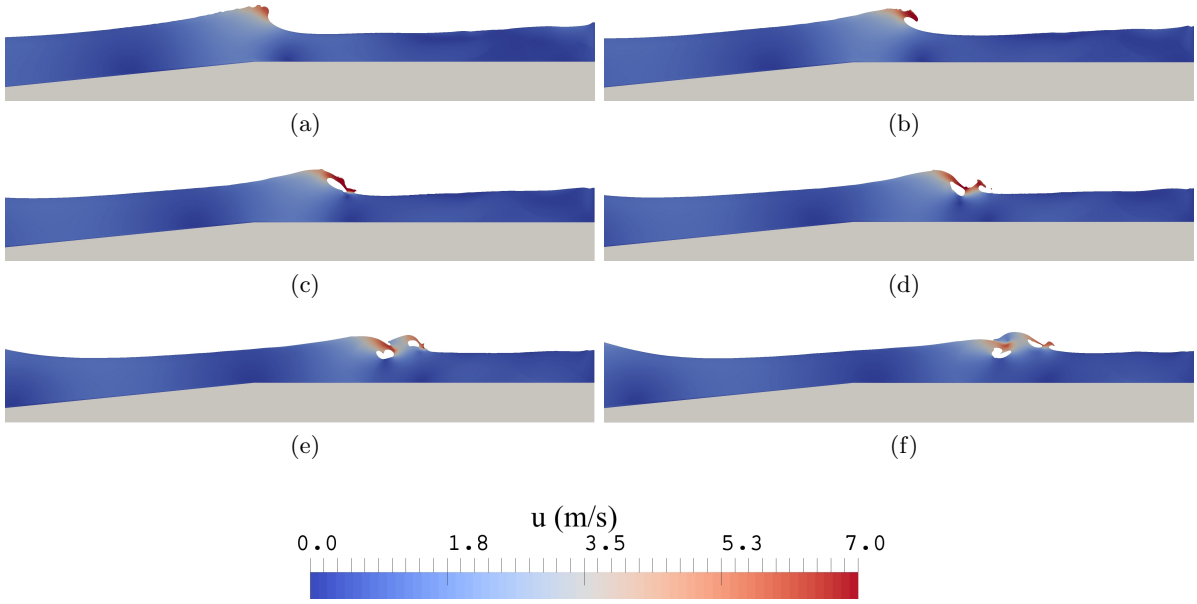


Figure 11: Computed wave profile with the horizontal velocity variation (m/s) during the wave propagation over sloping seabed (case S4) at (a) 22.7 s (b) 22.9 s (c) 23.05 s (d) 23.2 s (e) 23.27 s (f) 23.39 s

The present study investigates a total of 16 different wave loading scenarios with values of $x$ = 0.0 m (A1, B1, C1 and D1), 0.5 m (A2, B2, C2 and D2), 1.0 m (A3, B3, C3 and D3) and 1.5 m (A4, B4, C4 and D4). The alphabetic letters A, B, C and D are the cases with different wave steepnesses $s$ = 0.048, 0.051, 0.033 and 0.035, respectively, while numbers 1, 2, 3 and 4 indicate different locations of the front legs of the jacket $x$ = 0.0 m, 0.5 m, 1.0 m and 1.5 m, respectively (Fig. 12).

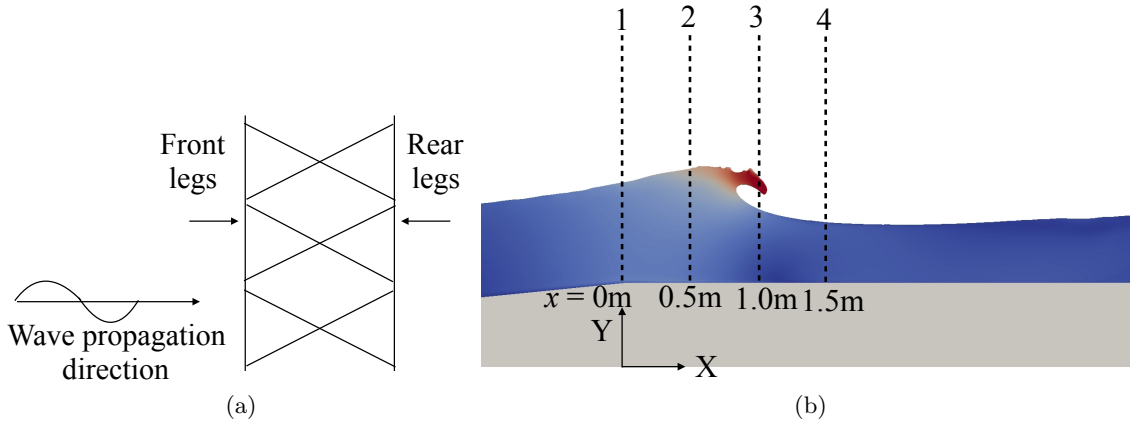


Figure 12: Different jacket locations with respect to the breaker (a) front and rear jacket legs (refer to Fig. 1c for jacket details) (b) different locations of the front legs of the jacket

**Free surface changes** In order to understand the breaking wave interaction with the jacket, the free surface changes at different time steps are presented in Fig. 13 for case D2 ($x = 0.5$ m, $s = 0.035$), where the wave breaks in the vicinity of the front legs of the jacket. It can be observed in Figs. 13a, 13b that as the waves propagate over the slope, they undergo wave shoaling until the wave crest becomes unstable and overturns signifying wave breaking (Figs. 13c and 13d). The interaction of the wave crest with the jacket also generates a highly turbulent free surface (Fig. 13d). The overturning wave crest develops further and interacts with the rear jacket structure and causes the secondary force peak (Figs. 13e and 13f). A breaking wave jet and a chute like phenomenon can be observed due to the interaction of the breaking wave crest with the rear legs of the jacket (Figs. 13g and 13h). On further propagation, the primary breaking wave jet rejoins the free surface and a secondary jet is generated due to the splash up phenomenon (Figs. 13i and 13j). This secondary wave jet is generated after the jacket and hence does not contribute towards the wave force for this case.

Fig. 14 presents the free surface changes at different time steps for case D4 ($x = 1.5$ m, $s = 0.035$). The front legs of the jacket are placed at $x = 1.5$ m from the location where wave breaking is initiated (Figs. 14a and 14b). Here, the fully developed overturning wave crest impacts the front legs of the jacket resulting in larger computed wave forces in this case than for case D2 ($x = 0.5$ m, $s = 0.035$). The overturning wave crest impacts the jacket with a large mass of water with large wave crest velocities (Figs. 14c and 14d). The semi-circular wave crest due to the wave-jacket interaction is less prominent in this case compared to case D2 (Fig. 13, $x = 0.5$ m, $s = 0.035$). The broken wave and the generated secondary wave jet interact with the rear jacket legs (Figs. 14e and 14f), and on further wave propagation, the secondary jet rejoins the free surface (Figs. 14g and 14h). The wave jacket interaction is quite different for the two wave impact scenarios presented above. The overturning wave crest on the front jacket legs leads to a larger primary peak of the wave impact force (case D2) compared to the vertical wave crest where wave breaking has just been initiated (case D4). Also, in case D4, the secondary wave jet generated as a result of the rejoining primary wave jet with the free surface also contributes to a secondary force peak unlike case D1, where the secondary jet is generated after the wave crest has propagated past the rear jacket legs. These features will be discussed further in the next section.

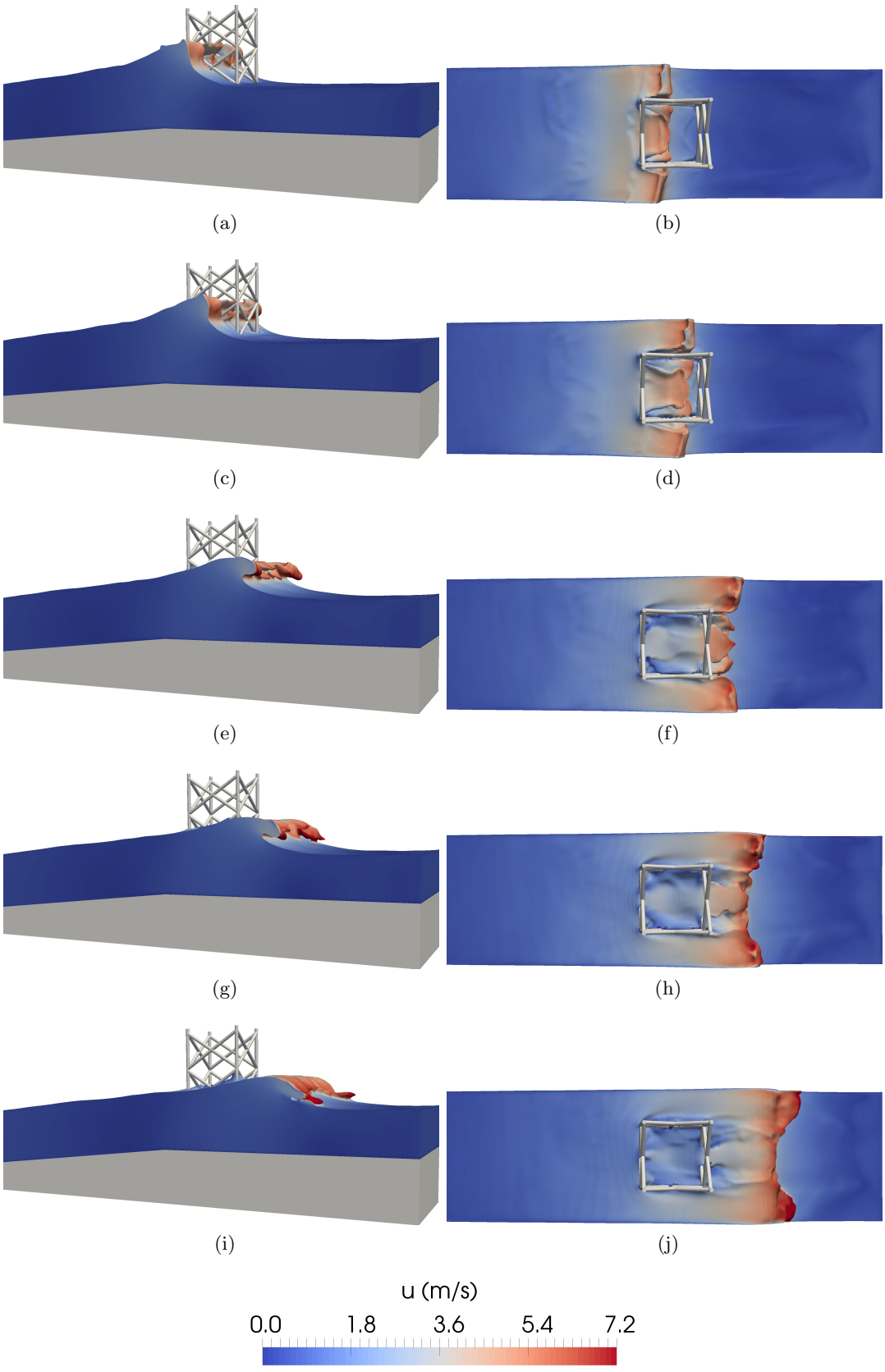


Figure 13: Computed wave profile during wave breaking with the velocity variation on the jacket for case D2 ($x = 0.5$ m, $s = 0.035$) at $t$ = (a) 34.5 s (isometric-view) (b) 34.5 s (top-view) (c) 35.05 s (isometric-view) (d) 35.05 s (top-view) (e) 35.20 s (isometric-view) (f) 35.20 s (top-view) (g) 35.35 s (isometric-view) (h) 35.35 s (top-view) (i) 35.50 s (isometric-view) (j) 35.50 s (top-view)

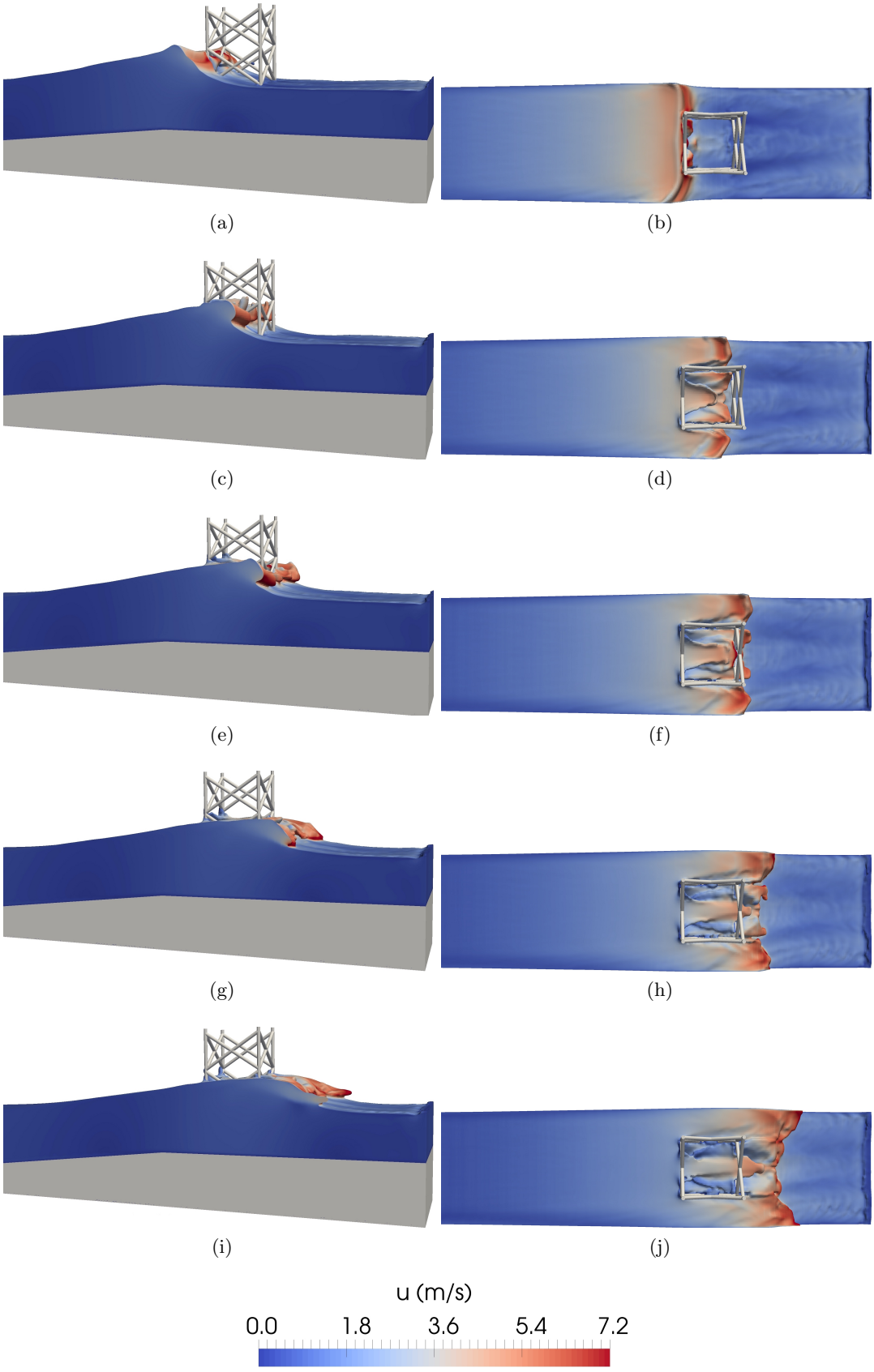


Figure 14: Computed wave profile during wave breaking with the velocity variation on the jacket for case D4 ($x = 1.5$ m, $s = 0.035$) at $t =$ (a) 28.9 s (isometric-view) (b) 28.9 s (top-view) (c) 29.05 s (isometric-view) (d) 29.05 s (top-view) (e) 29.20 s (isometric-view) (f) 29.20 s (top-view) (g) 29.35 s (isometric-view) (h) 29.35 s (top-view) (i) 29.50 s (isometric-view) (j) 29.50 s (top-view).

**Effect on wave forces** Fig. 15 presents the normalized total breaking wave force for different incident wave steepnesses with different jacket locations (cases A1-D4). For cases A1 ($x = 0.0$ m, $s = 0.035$), A2 ($x = 0.5$ m, $s = 0.035$), A3($x = 1.0$ m, $s = 0.035$) and A4 ($x = 1.5$ m, $s = 0.035$), the maximum first force peak is computed for case A3, because the overturning wave crest impacts the front legs of the jacket (Fig. 15a). When the waves impact the rear legs of the jacket, the waves have already broken as shown in Fig. 13, and hence the second force peaks are lower than the first force peaks for cases A1, A2, A3 and A4. For cases B1–D4, the wave breaking is initiated at the front legs of the jacket, but the overturning wave crest impacts the rear legs of the jacket due to which the second force peaks are larger than the first force peaks; the second forces peaks are maximum for cases B4 (Fig. 15b), C4 (Fig. 15c) and D4 (Fig. 15d). The overturning wave crests impact the rear legs of the jacket with a large mass of water (Figs. 13 and 14). The force peak values are lowest for cases A1 (Fig. 15a), B1 ((Fig. 15b)), C1 ((Fig. 15c)) and D1 ((Fig. 15d)), where waves are still shoaling and not breaking. In general, the force time plots for all cases exhibit two main peaks. The wave breaking location and impact of the overturning wave crest are the major factors which determine the magnitude of the peak breaking wave forces.

Figs. 16a and 16b present the normalized first and second force peaks versus the distance $x$. It can be observed that the value of the first force peak is highest for case A3 ($x = 1.0$ m), where the overturning wave crest impacts the front legs of the jacket; the increase in the peak magnitude is 40 % compared to case A1 ($x = 0.0$ m). In general, the first force peak value increases when the front legs of the jacket are located in the proximity of the overturning wave crest (Fig. 16a). The value of second force peak is highest for case D4, because the wave breaking location shifts further offshore, and the overturning wave crests impact the rear legs of the jacket. This value increases by 52 % on changing the $x$ from 0.0 m to 1.5 m. Also, the value of the second peaks is larger than the first force peaks for cases B1 – D4 (Fig. 16b). The variation of the first and second force peaks versus wave steepness is presented in Figs. 17a and 17b, respectively. Both first and second force peaks increase with the increment in wave steepness. When the wave steepness $s$ increases, the increase in the first force peak value with $s$ is largest for the impact scenario 1 ($x = 0.0$ m). The first force peak increases by 28 % at $s = 0.05$ compared to at $s = 0.03$ for the impact scenario 1 ($x = 0.0$ m). For the second force peaks, the effect of increasing $s$ is most noticeable for the impact scenario 4 ($x = 1.5$ m). The second force peak magnitude is larger by 61 % at $s = 0.05$ compared to at $s = 0.03$ for the impact scenario 4. This is due to both the higher incident wave energy (i.e., incident wave heights) and the impact of the overturning wave crest on the rear jacket legs.

**Statistics of breaking wave forces** In order to investigate the statistics of the breaking wave forces, the cumulative distribution functions (CDFs) for breaking wave forces are analysed. Fig. 18 presents the cumulative distribution functions (CDFs) for the normalized breaking wave force peaks $\hat{F}_b$. The breaking wave forces are normalized with their corresponding root-mean-square (rms) values. Two different distributions: the Weibull distribution and the lognormal distribution, are tested. The lognormal probability density function (PDF) is given by:

$$p(x) = \frac{1}{x\sigma_l\sqrt{2\pi}} exp\{-\frac{(\ln x - \mu_l)^2}{2\sigma_l^2}\} \tag{9}$$

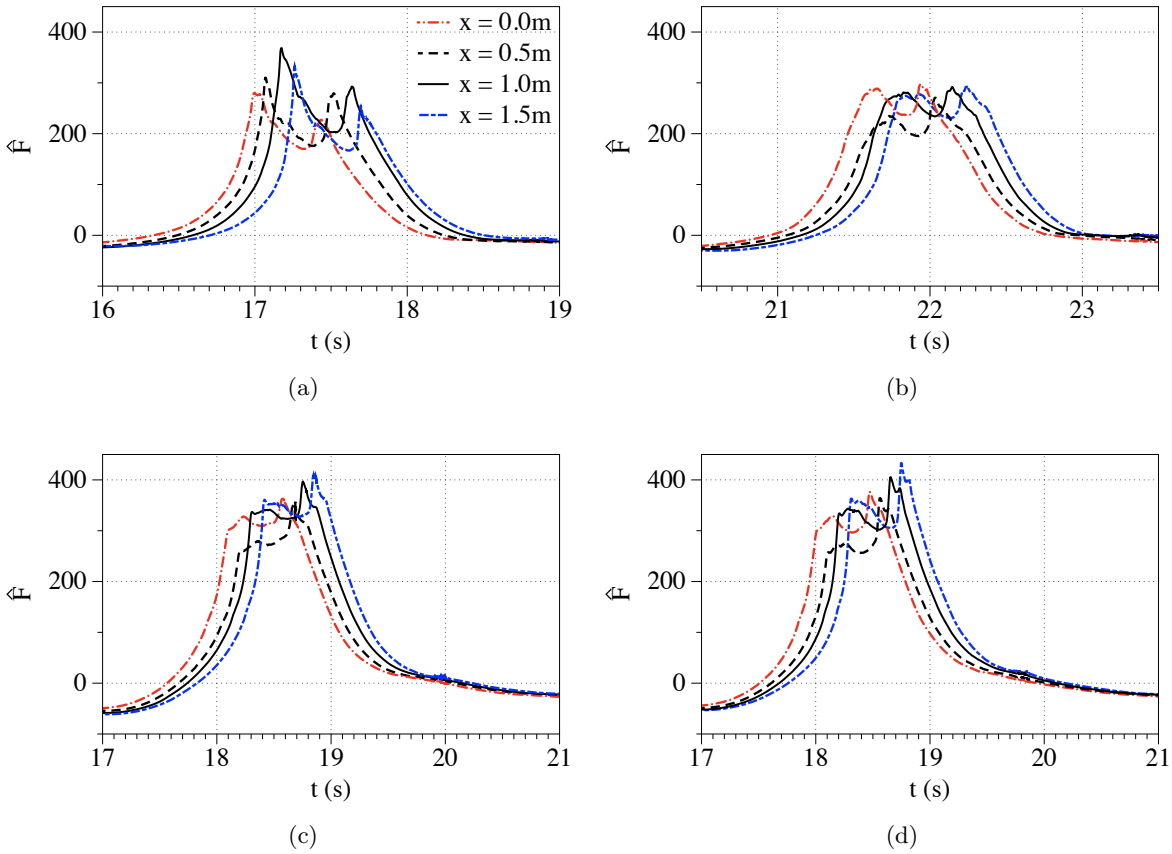


Figure 15: Time-variation of the normalized wave force $\hat{F}$ for cases (a) A1–A4 ($s = 0.048$) (b) B1–B4 ($s = 0.051$) (c) C1–C4 ($s = 0.033$) (d) D1–D4 ($s = 0.035$). Red dotted line for $x$ = 0 m; black dotted line for $x = 0.5$ m; black solid line for $x = 1.0$ m; blue dotted line for $x$ = 1.5 m.

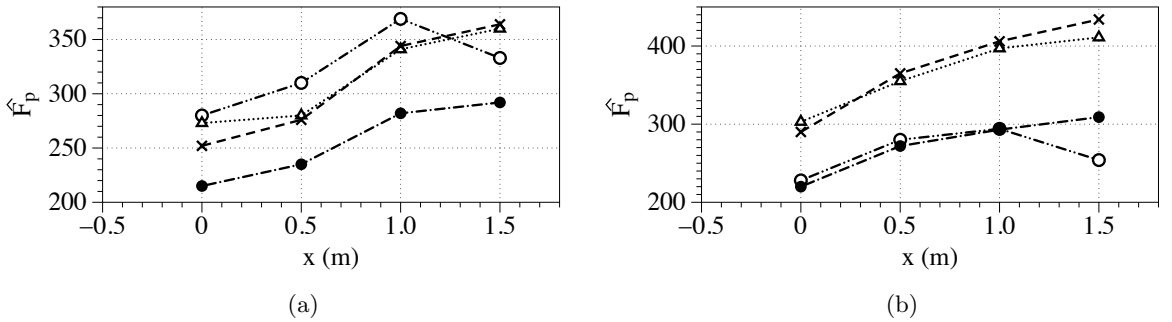


Figure 16: Variation of the normalized force peak $\hat{F_p}$ versus $x$ (a) first force peak (b) second force peak. White circles for $s = 0.048$ (case A); black circles for $s = 0.051$ (case B); triangles for $s = 0.033$ (case C); crosses for $s = 0.035$ (case D)

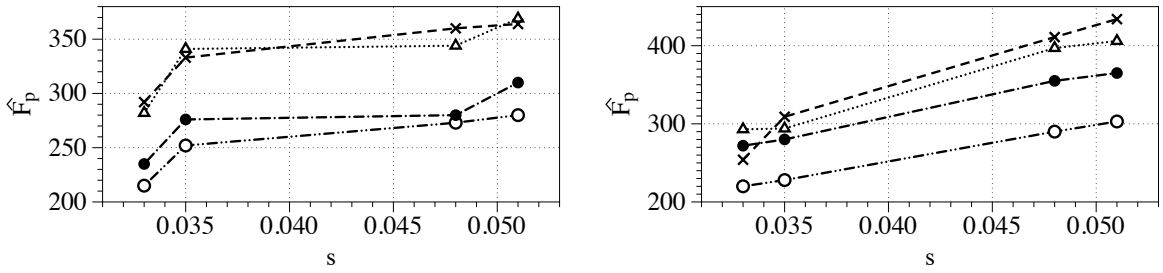


Figure 17: Variation of the normalized force peak $\hat{F_p}$ versus $s$ (a) first force peak (b) second force peak. White circles for $x = 0$ m; black circles for $x = 0.5$ m; triangles for $x = 1.0$ m; crosses for $x = 1.5$ m

where $\mu_l$ and $\sigma_l$ represent the log mean and log standard deviation of $x$, respectively; the best fit values of $\mu_l$ and $\sigma_l$ are given in Table 3.

The Weibull PDF is given by:

$$p(x) = \frac{b}{a}(\frac{x}{a})^{b-1} exp\{-(\frac{x}{a})^b\} \tag{10}$$

where b is the shape parameter and a is the scale parameter; the best fit values of a and b are presented in Table 3.

Figs. 18a and 18b indicate that the lognormal distribution is relatively more appropriate for both the first and second force peaks due to a better fit with the numerical data compared to the Weibull distribution. However, both the lognormal and the Weibull distributions are in reasonable fit with the data. This is also obvious by comparing the log-likelihood ($LL$) values in Table 3, *i.e.*, the $LL$ values can be used to compare the best fit between two distributions. A relatively higher $LL$ value gives a better distribution fit for the data (Kececioglu, 1993). However, both the first and second force peaks in the range of $\hat{F_b} = 0.92$-1 are not predicted correctly by any of the probabilistic distribution functions.

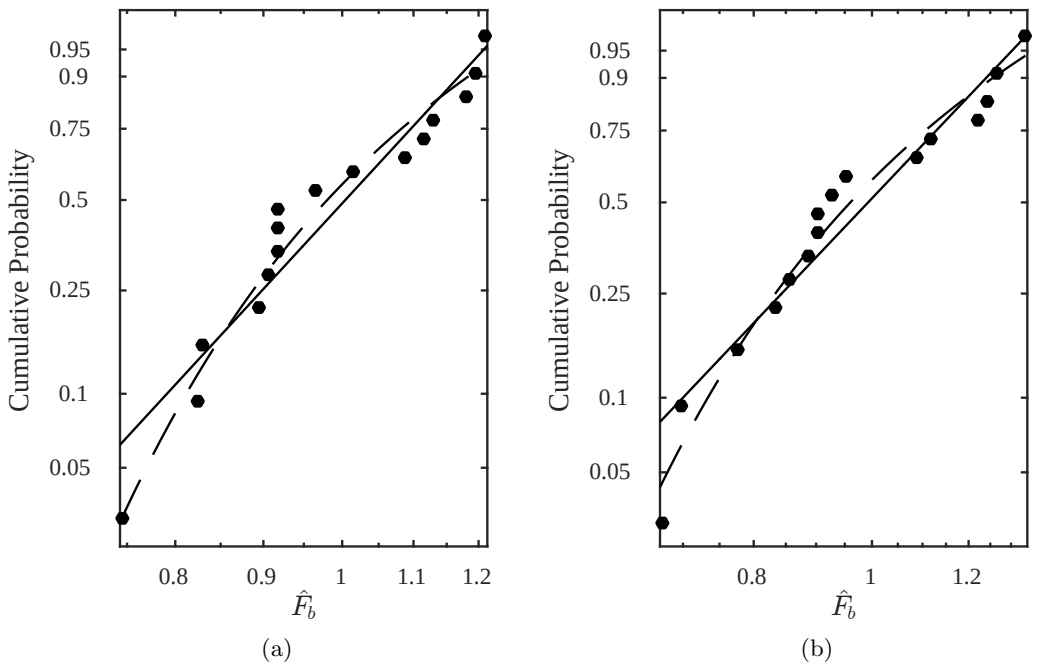


Figure 18: CDF fits in Weibull scale for the normalized (a) first force peaks; (b) second force peaks. Black circles for numerical data; black dashed line for lognormal fit; solid black line for Weibull fit (for details of the CDF fits, see Table 3)

**Evolution of wave harmonics** When waves propagate over sloping seabeds, they undergo wave shoaling, wave breaking and wave decomposition processes as explained above. During the wave transformation, their energy level at different frequencies change and higher wave harmonics are generated. Fig. 19 presents the evolution of the wave spectral density during wave shoaling (Fig. 19a) and wave breaking (Fig. 19b). The wave spectral density is normalized with the spectral peak value of the incident wave spectrum, and the frequency is normalized with the peak frequency $f_p$. It is observed in Fig. 19a that energy from the first-harmonic (H1) at $f/f_p = 1$ is transferred towards the second harmonic at $f/f_p = 2$ during wave shoaling, as waves propagate over the slope ($x$= -7 m). The value of H1 is reduced by almost 25 % and H2 is increased by almost 100 %. As the wave propagate further ($x$ = -5 m), H1 reduces further and major portion of the energy from H1 is transferred towards H2 and a minor portion towards H3 at $f/f_p = 3$. During wave breaking as shown in Fig. 19b, the contribution of higher-harmonics H2 and H3 in the spectral wave density increases further. A small energy transfer towards fourth-harmonic H4 at $f/f_p = 4$ is also observed. The first-harmonic peak H1 reduces by almost 70 % at $x$ = 5 m after wave breaking compared to the incident wave spectrum at $x$ = -28 m. Some of the incident wave energy is dissipated during wave breaking in form of turbulence and heat, while a certain portion of energy is transferred towards higher-harmonics (H2, H3 and H4). These phenomena of wave energy transfer and wave energy dissipation during wave shoaling and wave breaking can also be clearly noticed in Fig. 20, where the evolution of wave harmonics with the distance along the NWT is shown.

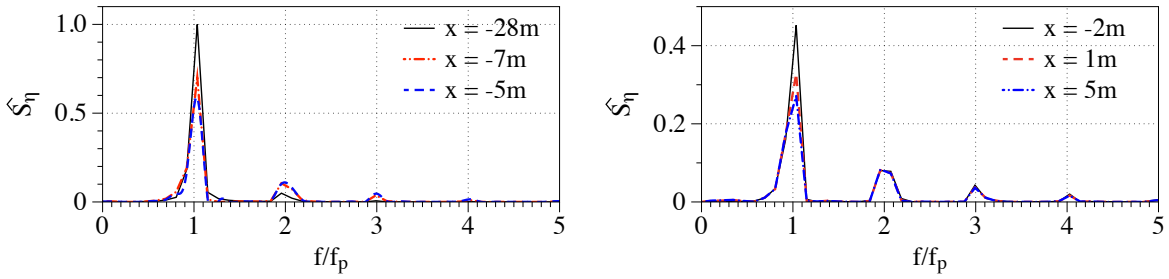


Figure 19: Evolution of wave spectral density over frequency for case A3 during (a) wave shoaling ($x$ = -28 m to -5 m) and (b) wave breaking ($x$ = -2 m to 5 m). $f_p$ is the peak frequency (0.22 Hz)

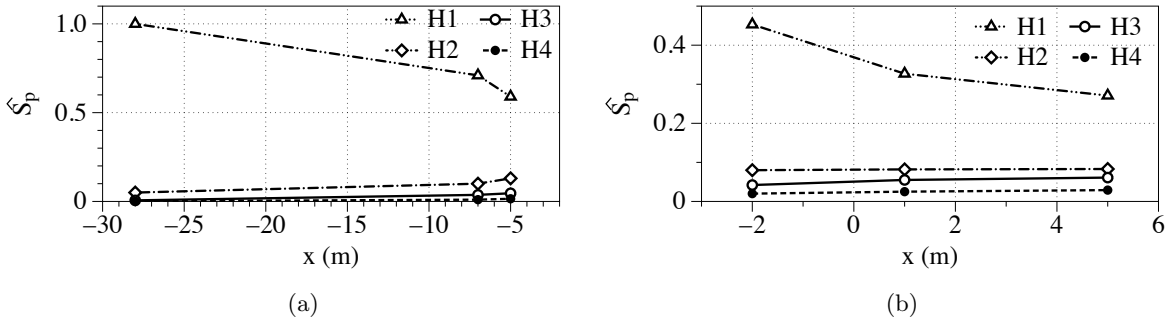


Figure 20: Evolution of wave harmonics over distance along the NWT for case A3 during (a) wave shoaling ($x$ = -28 m to -5 m) and (b) wave breaking ($x$ = -2 m to 5 m). $\hat{S}_p$ is the normalised spectral peak value; H1 is the first-harmonic at $f/f_p = 1$; H2 is the second-harmonic at $f/f_p = 2$; H3 is the third-harmonic at $f/f_p = 3$; H4 is the fourth-harmonic at $f/f_p = 4$

**Effect of the breaker location on wave-induced impact force rise time** Figs. 21a and 21b present the normalized rise times for both the first and second force peaks versus the distance $x$. The rise times are normalized with the total wave impact duration in each case. In general, the rise time for the first force peak decreases as the distance $x$ increases. The value of $t_r/t_d$ is highest for case B1, where the rise time of the first force peak is 28 % of the total impact duration (Fig. 21a). This value is least for case D4, where the rise time is only 19 % of the total impact duration. For the second force peak, $t_r/t_d$ is maximum, i.e., 10 % of the total wave impact duration for case C2 (Fig. 21b). In general, the rise time for the second force peak is not affected much by the change in jacket location. Further, the variations of the normalized rise times of the first and second force peaks versus the incident wave steepness are presented in Figs. 22a and 22b, respectively. The rise time for the first force peak is highest for the wave impact scenario B ($x$ = 0.5 m), where $t_r/t_d$ is 28 % of the total impact duration; $t_r/t_d$ is not affected much by changing the wave steepness $s$ for this wave impact scenario. For case D4, $t_r/t_d$ is minimum where the front legs of the jacket are

placed at $x = 1.5$ m with an incident wave steepness of $s = 0.035$ (Fig. 22a). For the second force peak, $t_r/t_d$ is maximum with $t_r/t_d = 10$ % of the total impact duration for $x = 1.0$ m (Fig. 22b).

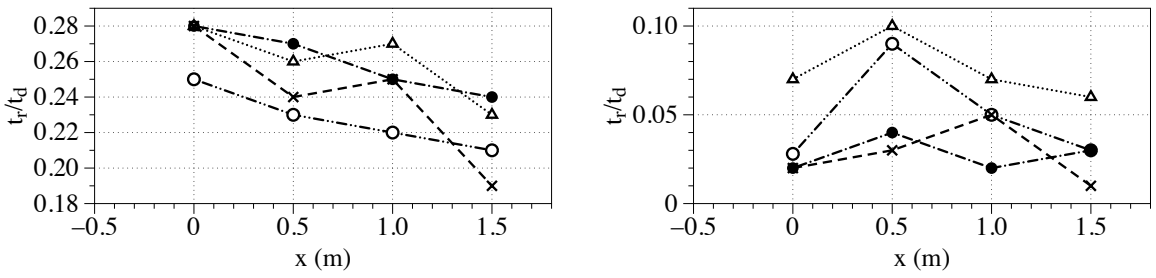


(a) (b)

Figure 21: Variation of the normalized rise time $t_r/t_d$ versus $x$ of the (a) first force peak (b) second force peak. White circles for $s = 0.048$ (case A); black circles for $s = 0.051$ (case B); triangles for $s = 0.033$ (case C); crosses for $s = 0.035$ (case D)

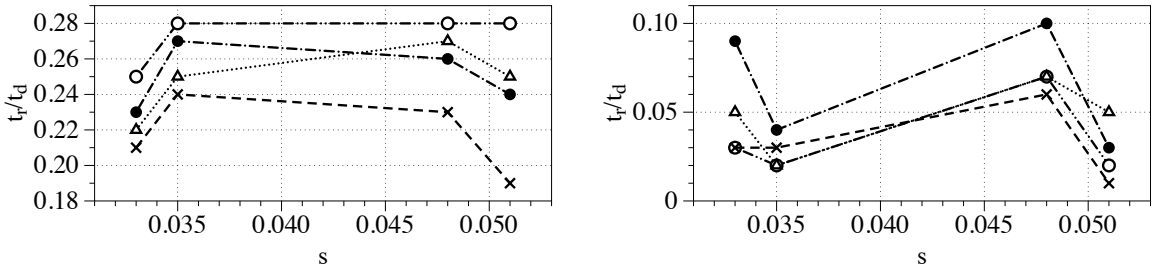


(a) (b)

Figure 22: Variation of the normalized rise time $t_r/t_d$ versus $s$ of the (a) first force peak (b) second force peak. White circles for $x = 0$ m; black circles for $x = 0.5$ m; triangles for $x = 1.0$ m; crosses for $x = 1.5$ m

Fig. 23 presents the CDFs for the normalized wave-induced impact rise time ($\hat{t_r}$) of both first (Fig. 23a) and second force peaks (Fig. 23b); $t_r$ is normalized with the rms value $t_{rms}$. Figs. 23a and 23b indicate that both the Weibull distribution and the lognormal distribution show a reasonable fit for the rise times of first and second force peaks (for details of the CDF fits, see Table 3). However, the Weibull distribution is slightly a better fit for the first force peaks, while, the lognormal distribution is slightly a better fit for the second force peaks.

**Spatial evolution of the horizontal velocity components during wave-jacket interaction** During the shoaling and breaking processes, the wave-induced velocities vary due to the change in water depth and wave heights. In order to understand this, the variations in the peak horizontal velocity components are investigated at different velocity probes located along the length of the NWT (Fig. 1a). Fig. 24 presents the normalized horizontal velocity

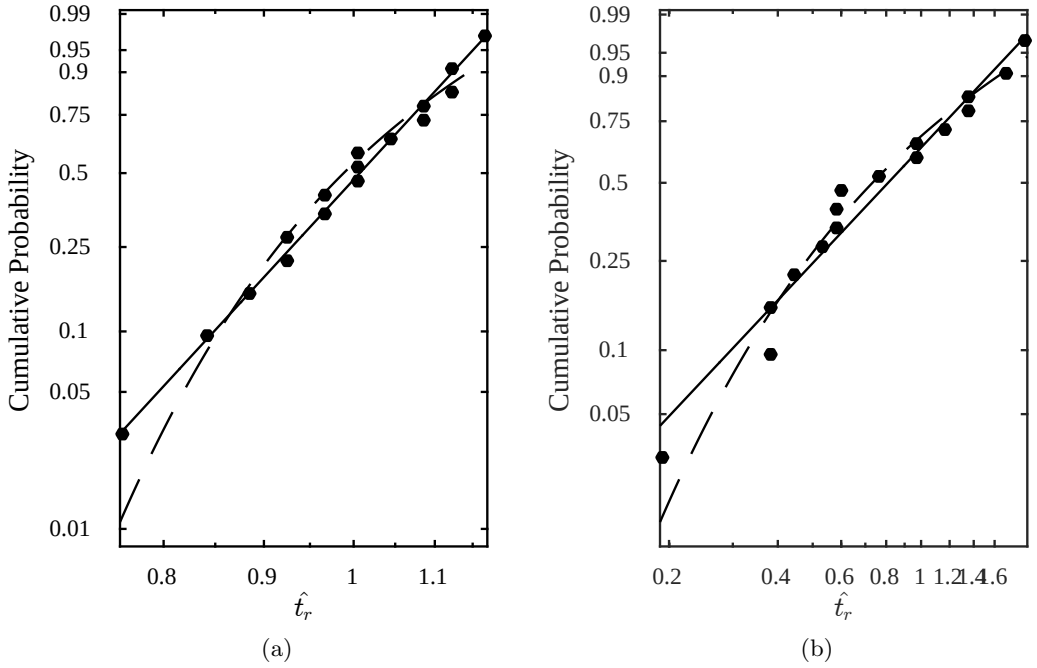


Figure 23: CDF fits in Weibull scale for the normalized wave-induced impact rise times of the (a) first force peak; (b) second force peak. Black circles for numerical data; black dashed line for lognormal fit; solid black line for Weibull fit (for details of the CDF fits, see Table 3)

versus the distance along the NWT for all 16 cases (case A1 to D4). In general, the normalized horizontal velocity $\hat{u}$ (normalized as in Eq. 6) increases during the wave shoaling process and reaches its maximum value at the fully developed wave breaker tongue during the wave breaking process. This can also be observed in Fig. 25. Fig. 24a shows that when the front legs of the jacket are mounted at $x = 0$ m (cases A1, B1, C1 and D1), the horizontal velocity values are highest for case B1 due to the largest wave steepness. This difference becomes significant for the maximum velocities, where $\hat{u}$ for case B1 (largest wave steepness) is larger by almost 29 % compared to case C1 (lowest wave steepness). When the wave breaker tongue impacts the jacket at these high velocities with a large mass of water, they exert a high impact force with a very short rise time (see Sec. 3.4.2). When the front legs of the jacket are placed at the toe of the flat part ($x = 0$ m), most of the wave breaking process occurs inside the jacket structure. When the jacket is placed at $x = 0.5$ m, the waves for case B2 reach their maximum wave height at the front legs of the jacket. The difference between the maximum of $\hat{u}$ for cases B2 and C2 becomes almost 26 % (Fig. 24b). The value of the maximum velocities for these cases with the jacket at $x = 0.5$ m is larger compared to the jacket at $x = 0.0$ m. When the front legs of the jacket are placed further away at $x = 1.0$ m (Fig. 24c) and at 1.5m (Fig. 24d), the difference between the maximum of $\hat{u}$ for cases B3-C3 and B4-C4 becomes 31 % and 22 %, respectively.

It can be noticed that the largest values of $\hat{u}$ is obtained, when the front legs of the jacket are placed at $x = 1.5$ m (cases A4, B4, C4 and D4) and the maximum value is obtained for case

B4 ($s = 0.051$). The horizontal velocity components at the front and rear legs and horizontal braces of the jacket are always larger compared to the horizontal velocity components outside the jacket structure. This phenomenon can be further noticed in Fig. 25 which presents the snapshots of the interaction of the breaking wave velocity vectors with the jacket at different time steps for case C3 ($x$=1.0 , $s$=0.033). The wave crest reaches its maximum height and impacts the front legs of the jacket as shown by the velocity vectors with larger velocities (Fig. 25a). When the wave crest further interacts with the jacket, it gains more momentum due to larger velocities and interacts with the horizontal braces of the jacket as seen in Figs. 25b and 25c. After the main wave crest has propagated past the rear legs of the jacket, the secondary jet propagating over the rear horizontal members reattaches to the main wave crest with the encasement of an air pocket during the reattachment process (Fig. 25d).

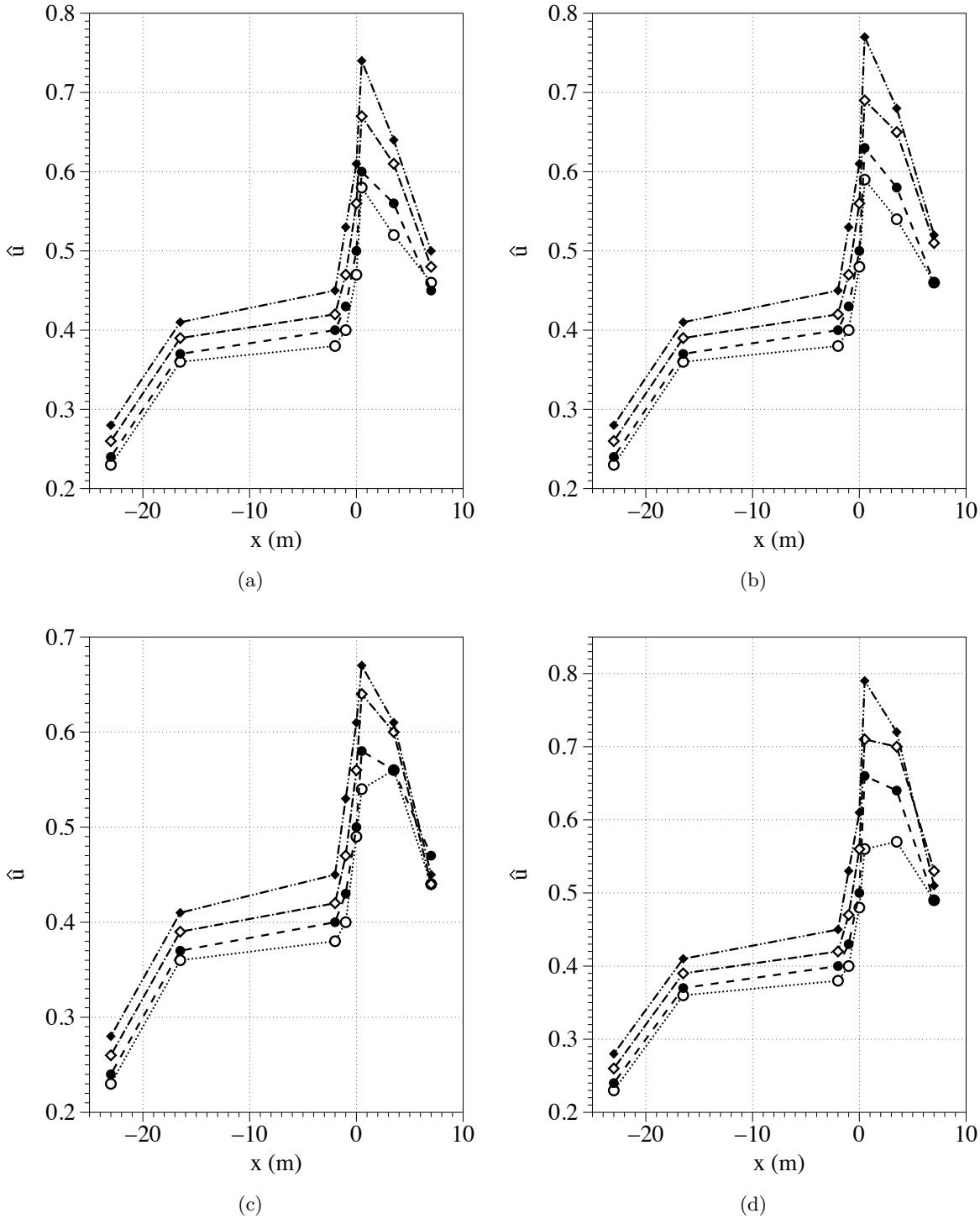


Figure 24: Variation of the horizontal velocity component during the breaking wave interaction with the jacket when the jacket is placed at (a) $x = 0$ m (cases A1, B1, C1 and D1); (b) $x = 0.5$ m (cases A2, B2, C2 and D2); (c) $x = 1.0$ m (cases A3, B3, C3 and D3); (d) $x = 1.5$ m (cases A4, B4, C4 and D4). White circles for $s = 0.033$; black circles for $s = 0.035$; white squares for $s = 0.048$; black squares for $s = 0.051$

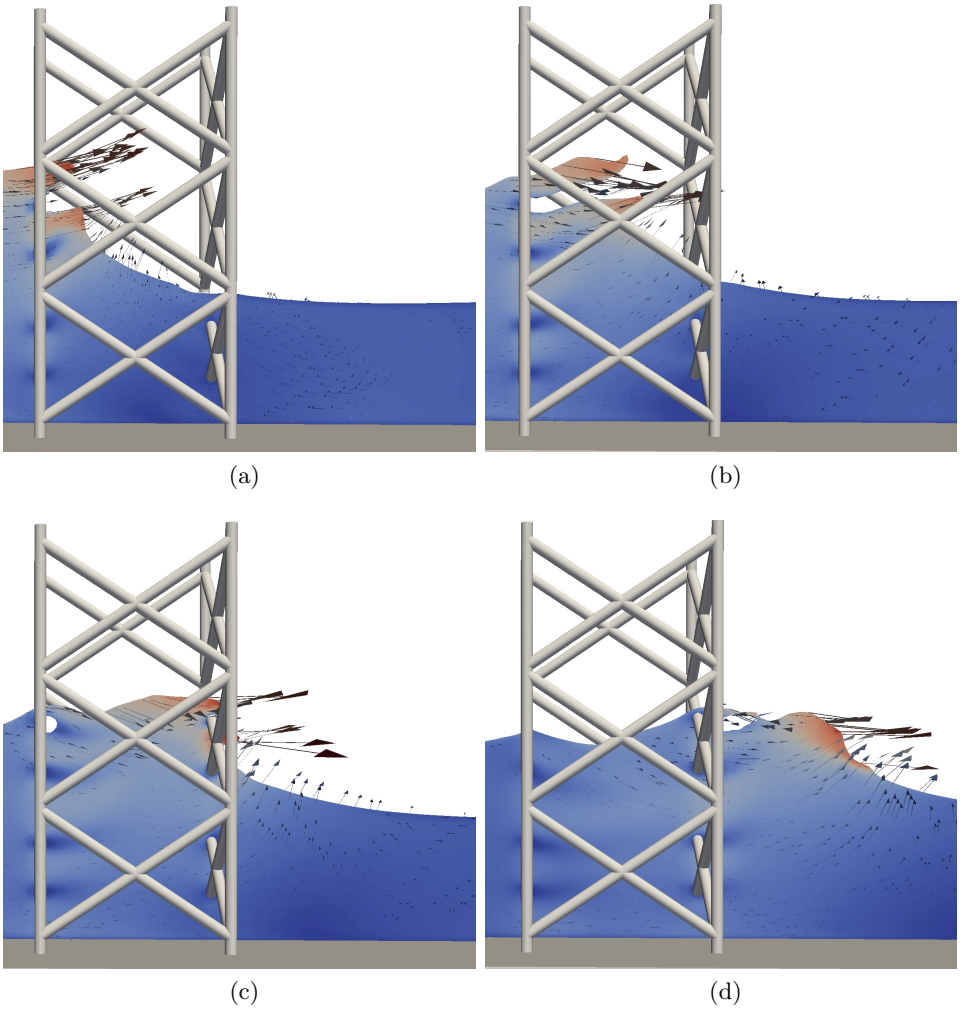


Figure 25: Vector representation of the wave velocity during the wave-jacket interaction for case C3 (x=1.0 , s=0.033) at (a) $t$ = 19.06 s (b) 19.22 s (c) 19.48 s (d) 20.09 s

Fig. 26 presents the CDFs for the normalized horizontal velocity component ($\hat{u}$), here $u$ is normalized with its rms value $u_{rms}$ at the wave breaker tongue (maximum velocity) (Fig. 26a) and after the splash up phenomenon (Fig. 26b). Figs. 26a and 26b indicate that the lognormal distribution gives the best fit for $\hat{u}$ compared to the Weibull distribution at the both velocity probe locations (at the wave breaker tongue and after the splash up). However, it can be clearly observed in Fig. 26b and from the values given in Table 3, that the value of standard deviation is larger for the velocity measurements after wave breaking. This could be due to the possible wave non-linearity and wave decomposition processes occurring as a result of wave breaking.

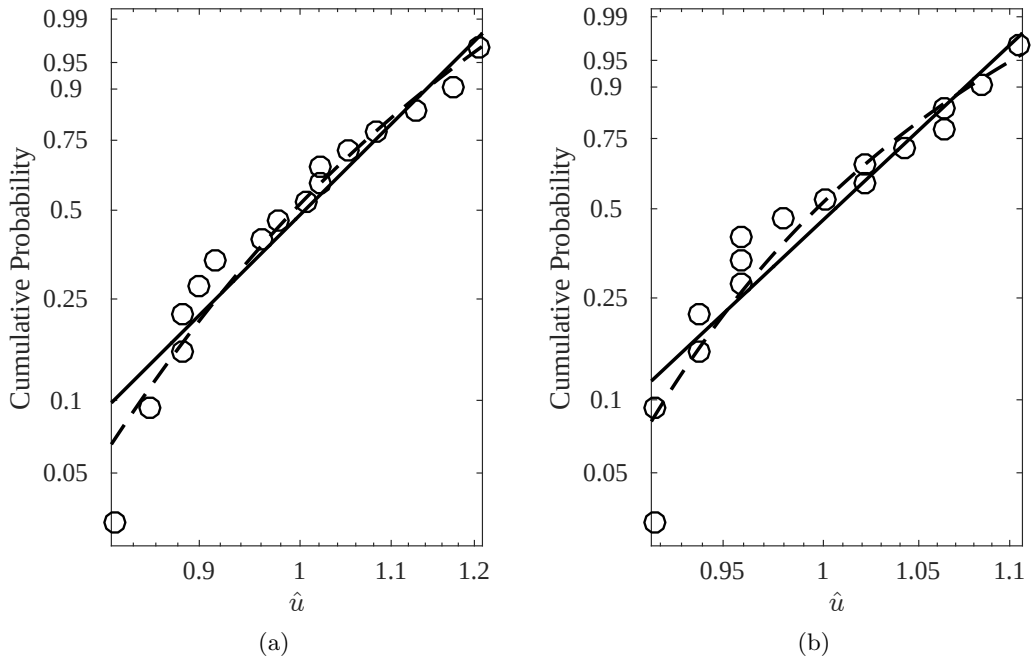


Figure 26: CDF fits in Weibull scale for the normalized peaks of the horizontal velocity component (a) at the breaker tongue (maximum values); (b) after wave breaking. White circles for numerical data; black dashed line for lognormal fit; solid black line for Weibull fit (for details of the CDF fits, see Table 3)

| | Weibull | | | Lognormal | | |
|---|---|---|---|---|---|---|
| | a | b | LL | $\sigma_l$ | $\mu_l$ | LL |
| Normalized maximum horizontal velocity | 0.68 | 9.43 | 18.40 | -0.43 | 0.11 | 19.45 |
| Normalized horizontal velocity post breaking | 0.49 | 18.01 | 33.51 | -0.74 | 0.06 | 34.45 |
| Normalized first force peak | 0.51 | 13.43 | 26.78 | -0.52 | 0.05 | 27.67 |
| Normalized second force peak | 0.67 | 19.23 | 15.67 | -0.79 | 0.13 | 18.97 |
| Normalized rise time for first force peak | 1.04 | 11.00 | 13.38 | -0.11 | 0.11 | 12.68 |
| Normalized rise time for second force peak | 0.98 | 1.87 | -9.93 | -0.31 | 0.03 | -9.75 |

Table 3: Table listing the details for different statistical parameters for the Weibull and lognormal distributions

# 4 Conclusions

A two-phase CFD model is used for the numerical investigation of breaking wave forces on a jacket structure mounted on a slope. The numerical model is validated by performing a grid convergence study for breaking regular wave free surface elevation. The numerical results for the free surface wave elevation at different wave gauge locations and total breaking wave forces are compared with the experiments by Arntsen and Gudmestad (2014) and a good agreement is obtained with the experimental data for the free surface elevation and the wave force. An extensive numerical analysis is performed in a two-dimensional (2D) numerical wave tank (NWT) with different wave steepness cases to investigate the breaking characteristics including breaker indices and geometric profile properties. The wave breaking location and incident wave parameters play an important role in influencing the breaker indices and geometric profile properties.

Further, the numerical analysis is performed in a 3D NWT to investigate the effect of the breaker location on the slamming wave loads for 16 different cases with different incident wave steepnesses at different locations of the front face of the jacket with respect to the breaking point. Further, the role of the wave breaking location, the overturning wave crest and the horizontal velocity component on the force peaks and their rise times is investigated. The following conclusions can be drawn from the study:

- In general, the breaker height index and breaker depth index decrease, when the wave breaking location shifts farther onshore. Also, the waves undergo more deformation due to more interaction of wave crests with the slope as noticed by the decrease in the crest front wave steepness, crest rear wave steepness and horizontal asymmetry factor as the wave breaking shifts onshore.

- The primary force peak is highest when the overturning wave crest impacts the front legs of the jacket compared to the cases when front legs of the jacket are mounted at the location where the wave crest is vertical and the wave breaking is initiated. As, expected the primary force peak is larger for the cases with larger wave steepnesses.

- Generally, the second force peak is highest when the front legs of the jacket are placed at a distance of 1.5 m from the toe end of the slope. Here, the overturning wave crests impact the rear legs of the jacket and thus, a larger second force peaks.

- The normalized relative rise times of the first and second force peaks are strongly dependent on the location of the jacket with respect to the breaking point. In general, the rise times are shortest when the front legs of the jacket are placed at a distance of 1.5 m from the toe end of the slope.

- When waves propagate over sloping seabeds, the contribution of the first harmonic peak in the wave spectrum decreases by almost 70 % after wave breaking compared to the incident wave spectrum. This wave energy is dissipated during wave breaking in form of turbulence and heat, while a certain portion of the energy is transferred towards higher-harmonics (i.e., associated with the second, third and fourth peaks in the wave spectrum).

- When the overturning wave crests reunite with the free surface, a secondary water jet is generated due to the splash up phenomenon. This secondary water jet contributes to the second force peaks for the cases when it impacts the rear jacket legs. In general, a highly turbulent free surface is observed around the jacket legs during the wave jacket interaction process.
- The lognormal distribution can be used to estimate the statistics of horizontal velocity components and both the first and second breaking wave force peaks during the wave-jacket interaction. Both the Weibull and the lognormal distributions show reasonable fits for the rise times of both the first and second force peaks.

## Acknowledgements

The research work has been funded by the Research Council of Norway through the project "Hydrodynamic Loads on Offshore Wind Turbine Substructures" (project number: 246810). The authors gratefully acknowledge the computing time granted by NOTUR (project number: NN2620k).

## References

Aashamar, M. (2012). Wave slamming forces on truss support structures for wind turbines. *Master's Thesis, Norwegian University of Science and Technology, Trondheim, Norway.*

Aggarwal, A., Alagan Chella, M., Bihs, H., Pakzodi, C., P., A.B. and Arntsen, A.Ø.. (2018*a*). CFD-based study of steep irregular waves for extreme wave spectra. *International Journal of Offshore and Polar Engineering*, **28(2)**, 164–170.

Aggarwal, A., Alagan Chella, M., Kamath, A., Bihs, H. and Arntsen, A.Ø. (2016). Irregular wave forces on a large vertical circular cylinder. *Energy Procedia*, **94**, 504–516.

Aggarwal, A., Pákozdi, C., Bihs, H., Myrhaug, D. and Alagan Chella, M. (2018*b*). Free surface reconstruction for phase accurate irregular wave generation. *Journal of Marine Science and Engineering*, **6(3)**, doi:10.3390/jmse6030105.

Ahmad, N., Bihs, H., Myrhaug, D., Kamath, A. and Arntsen, Ø..A. (2018). Three-dimensional numerical modelling of wave-induced scour around piles in a side-by-side arrangement. *Coastal Engineering*, **138**, 132–151.

Alagan Chella, M., Bihs, H., Myrhaug, D. and Michael, M. (2017). Breaking solitary waves and breaking wave forces on a vertically mounted slender cylinder over an impermeable sloping seabed. *Journal of Ocean Engineering and Marine Energy*, **3(1)**, 1–19.

Apelt, J.C. and Piorewicz, J. (1987). Laboratory studies of breaking wave forces acting on vertical cylinders in shallow water. *Coastal Engineering*, **11**, 263–282.

Arntsen, A.Ø.. and Gudmestad, O.T. (2014). Wave slamming forces on truss structures in shallow water. *Proceedings of the HYDRALAB IV Joint User Meeting, Lisbon.*

Berthelsen, P.A. and Faltinsen, O.M. (2008). A local directional ghost cell approach for incompressible viscous flow problems with irregular boundaries. *Journal of Computational Physics*, **227**, 4354–4397.

Bihs, H. and Kamath, A. (2017). A combined level set/ghost cell immersed boundary representation for floating body simulations. *International Journal for Numerical Methods in Fluids*, **83(12)**, 905–916.

Bihs, H., Kamath, A., Alagan Chella, M., Aggarwal, A. and Arntsen, A.Ø. (2016*a*). A new level set numerical wave tank with improved density interpolation for complex wave hydrodynamics. *Computers and Fluids*, **140**, 191–208.

Bihs, H., Kamath, A., Alagan Chella, M. and Arntsen., A.Ø. (2016*b*). Breaking-wave interaction with tandem cylinders under different impact scenarios. *Journal of Waterway, Port, Coastal, and Ocean Engineering*, **142(5)**, 1–14.

Bredmose, H. and Jacobsen, N.G. (2010). Breaking wave impacts on offshore wind turbine foundations: focused wave groups and cfd. In: *ASME 2010 29th International Conference on Ocean, Offshore and Arctic Engineering*, 397–404. American Society of Mechanical Engineers.

Bredmose, H. and Jacobsen, N.G. (2011). Vertical wave impacts on offshore wind turbine inspection platforms. In: *ASME 2011 30th International Conference on Ocean, Offshore and Arctic Engineering*, 645–654. American Society of Mechanical Engineers.

Burmester, S., de Ridder, E.J., Wehmeyer, C., Asp, E. and Gujer, P. (2017). Comparing different approaches for calculating wave impacts on a monopile turbine foundation. In: *ASME 36th International Conference on Ocean, Offshore and Arctic Engineering*.

Choi, S., Lee, K. and Gudemestad, O. (2015). The effect of dynamic amplification due to a structures vibration on breaking wave impact. *Ocean Engineering*, **96**, 8–20.

Chorin, A.J. (1968). Numerical solution of the Navier-Stokes equations. *Mathematics of Computation*, **22**, 745–762.

Christensen, E.D. (2006). LES simulation of spilling and plunging breakers. *Coastal Engineering*, **53**, 463–485.

Christensen, E.D., Bredmose, H. and Hansen, E.A. (2005). Extreme wave forces and wave run-up on offshore wind turbine foundations. *Proceedings of Copenhagen Offshore Wind*, 1–10.

Damiani, R., Dykes, K. and Scott, G. (2016). A comparison study of offshore wind support structures with monopiles and jackets for US waters. *Journal of Physics:Conference Series*, **753(9)**, 092003.

De Vries, W., Vemula, N.K., Passon, P., Fischer, T., Kaufer, D., Matha, D., Schmidt, B. and Vorpahl, F. (2011). Final report wp 4.2: support structure concepts for deep water sites: deliverable d4. 2.8 (wp4: offshore foundations and support structures).

EWEA (2015). The european offshore wind industry—key trends and statistics 2014 tech. rep. *European Wind Energy Association*.

Falgout, R.D. and Yang, U.M. (2002). HYPRE: A library of high performance preconditioners. **Springer Berlin Heidelberg**, 632–641.

Goda, Y., Haranaka, S. and Kitahata, M. (1966). Study of impulsive breaking wave forces on piles. *Report of Port and Harbor Research Institute*, **5(6)**, 1–30.

Griebel, M., Dornseifer, T. and Neunhoeffer, T. (1998). *Numerical Simulations in Fluid Dynamics*. SIAM.

Hieu, D., Katsutoshi, T. and Ca, T.V. (2004). Numerical simulation of breaking waves using a two-phase flow model. *Applied Mathematics Modelling,*, **28**, 983–1005.

Hildebrandt, A. and Schlurmann, T. (2012). Breaking wave kinematics, local pressures, and forces on a tripod structure. *Coastal Engineering Proceedings*, **1(33)**, 71.

Irschik, K., Sparboom, U. and H., O. (2004). Breaking wave loads on a slender pile in shallow water. *Coastal Engineering*, **1**, 568–580.

Jacobsen, N.G., Fuhrman, D. and Fredsøe, J. (2012). A wave generation toolbox for the open-source CFD library: Openfoam®. *International Journal for Numerical Methods in Fluids*, **70**, 1073–1088.

Jiang, J. and Shu, C.W. (1996). Efficient implementation of weighted eno schemes. *Journal of Computational Physics*, **126**, 202–228.

Jose, J. and Choi, S. (2017). Estimation of slamming coefficients on local members of offshore wind turbine foundation (jacket type) under plunging breaker. *International Journal of Naval Architecture and Ocean Engineering*, **1**, 1–17.

Jose, J., Podrazka, O., Obhrai, C., Gudmestad, O. and Cieslikiewicz, W. (2016). Methods for analysing wave slamming loads on truss structures used in offshore wind applications based on experimental data. *Journal of Offshore and Polar Engineering*, **26(2)**, 100–108.

Kamath, A., Alagan Chella, M., Bihs, H. and Arntsen, A., Ø. (2016). Breaking wave interaction with a vertical cylinder and the effect of breaker location. *Ocean Engineering*, **128**, 105–115.

Kececioglu, D. (1993). Reliability and life testing handbook. *Prentice Hall*.

Kjeldsen, S.P. and Myrhaug, D. (1978). Kinematics and dynamics of breaking waves. *Technical Report. River and Harbour Laboratory. The Norwegian Institute of Technology, Trondheim, Norway.*, **STF60A78100**.

Lin, P. and Liu, L. (1998). A numerical study of breaking waves in the surf zone. *Journal of Fluid Mechanics*, **359**, 239–264.

Loukogeorgaki, E., Lentsiou, E. and Chatjigeorgiou, I. (2016). Experimental investigation of slamming loading on a three-legged jacket support structure of offshore wind turbines. *Proceedings of 26th International Ocean and Polar Engineering Conference, International Society of Offshore and Polar Engineers*, **1**, 192–198.

Mayer, S., Garapon, A. and Sø rensen, S.L. (1998). A fractional step method for unsteady free surface flow with applications to non-linear wave dynamics. *International Journal of Numerical Mathematics and Fluids*, **28**, 293–315.

Mo, W., Jensen, A. and Liu, P. (2013). Plunging solitary wave and its interaction with a slender cylinder on a sloping beach. *Ocean Engineering*, **74**, 48–60.

Musial, W., Butterfield, S., Ram, B. et al. (2006). Energy from offshore wind. In: *Offshore technology conference*. Offshore Technology Conference.

Osher, S. and Sethian, J.A. (1988). Fronts propagating with curvature- dependent speed: Algorithms based on hamilton-jacobi formulations. *Journal of Computational Physics*, **79**, 12–49.

Ros, C. (2011). Impact forces on a vertical pile from plunging breaking waves. *Master's Thesis, Norwegian University of Science and Technology, Trondheim, Norway.*

Sarpkaya, T. (1979). Wave impact loads on cylinders. *Society of Petroleum Engineers Journal*, **19(1)**, 29–36.

Sawaragi, T. and Nochino, M. (1984). Impact forces of nearly breaking waves on a vertical circular cylinder. *Coastal Engineering in Japan*, **27(1)**, 249–263.

Shu, C.W. and Oscher, S. (1988). Efficient implementation of essentially non-oscillatory shock capturing schemes ii. *Journal of Computational Physics*, **77**, 439–471.

Tanimoto, K., T.S.K.T. and Shiota, K. (1986). Impulsive breaking wave forces on an inclined pile exerted bi random waves. *Proceedings of the 20th Conference on Coastal Engineering.*

Wienke, J., Sparboom, U. and Oumeraci, H. (2000). Breaking wave impact on a slender cylinder. *Coastal Engineering Conference*, 1787–1798.

Wilcox, D. (1994). Turbulence modeling for CFD. *DCW Industries Inc. La Canada, California.*

Ying, T., Cheng, Z. and Muskulus, M. (2018). Global slamming forces on jacket structures for offshore wind applications. *Marine Structures*, **58**, 53–72.

Zhao, Q., Armfield, S. and Tanimoto, K. (2004). Numerical simulation of breaking waves by a multi-scale turbulence model. *Coastal Engineering*, **51**, 53–80.